Optimization of the Bowtie Gap Geometry for a Maximum Electric Field Enhancement

Tsenguun Byambadorj
Marquette University

OPTIMIZATION OF THE BOWTIE GAP GEOMETRY FOR A MAXIMUM ELECTRIC FIELD ENHANCEMENT

by

Tsenguun Byambadorj, B.S.

A Thesis submitted to the Faculty of the Graduate School,
Marquette University,
in Partial Fulfillment of the Requirements for
the Degree of Master of Science

Milwaukee, Wisconsin

December 2016

ABSTRACT
OPTIMIZATION OF THE BOWTIE GAP GEOMETRY FOR A MAXIMUM ELECTRIC FIELD ENHANCEMENT

Tsenguun Byambadorj, B.S.

Marquette University, 2016

Optimization of the geometry of a metallic bowtie gap at radio frequency is presented in this thesis. Since the design and fabrication of a plasmonic device (nanogap) at nanoscale is challenging, the results of this study can be used to estimate the best design parameters for nanogap structure. The geometry of the bowtie gap including gap size, tip width, metal thickness, and tip angle are investigated at macroscale to find the maximum electric field enhancement across the gap. This thesis focuses on the simulation portion of a work that consists of experimental and simulation platforms.

The simulation platform is created by NEC modeling system using antenna segments. The results indicate that 90° bowtie with 0.06 λ gap size has the most $|E_t|^2$ enhancement. Different amounts of enhancement at different frequency ranges are explained by mode volume. The product of the mode volume and $|E_t|^2$ enhancement is constant for different gap structures and different frequencies.

ACKNOWLEDGEMENTS

Tsenguun Byambadorj, B.S.

I would like to take this opportunity to thank my parents Byambadorj Jamiyan, Batkhishig Shinen, and brother Bilguun Byambadorj for their love and support since the day I was born.

The completion of my Master of Science degree and other accomplishments would not have been possible without the persistent guidance and teaching of my advisors Dr. Chung Hoon Lee and Dr. James E. Richie. I would also like to thank the former and current members of the Nanoscale Device Laboratory, MohamadAli Malakoutian, HyeJeong Bak, Michael Bachmann, and especially Dr. Benyamin Davaji, for their valuable collaboration and assistance.

In addition, I thank the committee members of my M.S thesis, Dr. Edwin Yaz and Mr. Benjamin Koch, for their constructive criticism and feedback.

I am grateful for this opportunity provided by Marquette University's Department of Electrical and Computer Engineering.

Tsenguun Byambadorj

Milwaukee, WI

Table of Contents

ACKNOWLEDGEMENTS i

LIST OF TABLES v

LIST OF FIGURES vi

CHAPTERS

1. Introduction 1

1.1 Motivation 1

1.2 Subwavelength Imaging Techniques 2

1.3 Near-field Imaging 3

1.4 Objective of Thesis 5

1.5 Thesis Outline 6

2. Subwavelength Imaging and Plasmonics 7

2.1 Single Cell Imaging 7

2.2 Single Molecule Imaging 10

2.3 Diffraction Limit 12

2.4 Near-Field Scanning Optical Microscopy (NSOM) 17

2.4.1 Force-Based Near-Field Imaging 17

2.4.2 Optical-Based Near-Field Imaging 18

2.5 Raman Spectroscopy 19

2.5.1 Surface-Enhanced Raman Spectroscopy 25

2.6 Plasmons 26

2.6.1 Localized Surface Plasmons 28

2.6.2 Coupling of Localized Surface Plasmons 31

2.7 Optimization of Electric Field Enhancement 36

3. Macroscale Experiment and NEC Modeling 37

3.1 Difficulties in Nanoparticle Fabrication 37

3.2 Macroscale Enhancement Experiment 39

3.3 Previous Work 40

3.4 Approach of the Thesis 43

3.5 Modeling of the Experimental Components 46

4. Electric Field Simulations and Results 52

4.1 Electric Field Simulation 52

4.1.1 Electric Field Enhancement 53

4.2 Geometry Effect on Enhancement Factor 55

4.2.1 Tip Angle 57

4.2.2 Gap Size 59

4.2.3 Thickness 60

4.3 Mode Volume 61

5. Conclusion and Future Work 65

5.1 Conclusion.....65

5.2 Future Work 66

BIBLIOGRAPHY 68

Appendix A: Published Journal Paper 74

LIST OF TABLES

Table 2-1: Examples of Raman Frequencies of some organic compounds. 23

Table 2-2 Plasma frequencies and wavelengths of metals commonly used for LSPR applications [44].....30

Table 2-3 Electric field enhancement factors for gold nanospheres and nanoshells in different configurations [20].....33

Table 3-1 Variant geometry parameters of the bowtie 44

Table 4-1 Comparison of the maximum enhancement factors and the respective gap sizes found by simulation and experiment.....56

Table 4-2 The maximum enhancement gap sizes of the 90° bowtie at different incident field frequencies.....59

Table 4-3 The maximum enhancement factor and gap size of the 1/8”, 1/4”, and 3/8” thick 90° bowtie structures. 61

Table 4-4 The volumetric enhancement factors in macroscale and nanoscale. 64

LIST OF FIGURES

Figure 2-1 a) Normal Yeast Cell under Conventional Optical Microscope, b) Yeast cell membrane visualized by membrane proteins fused with RFP and GFP fluorescent markers [Public Domain Figure]. 9

Figure 2-2 Phase Contrast Microscopy Image of Yeast Cell Division [Public Domain Figure].....10

Figure 2-3 Plane Wave that Consists of Individual Hyegens' Wavelets Forming a Planar Wavefront [31].....12

Figure 2-4 Single-Slit Diffraction Pattern [Public Domain Figure]. 14

Figure 2-5 Double-Slit Constructive and Destructive Pattern [Public Domain Figure]....14

Figure 2-6 The intensity distributions of Airy discs. a) A single Airy disc, b) Non-overlapping Airy discs as a result of distinguishable objects, c) Overlapping Airy discs as a result of indistinguishably close objects [33].....16

Figure 2-7 Raman Scattering of Graphene [35]. The intensity peaks allow distinguish the quality of graphene. 21

Figure 2-8 Raman spectra energy level diagram (Rayleigh, Stokes, anti-Stokes) [36].....24

Figure 2-9 Detailed view of the effect of physical location on the electromagnetic field enhancement |E| in gold nanoparticles. a) Single nanosphere, b) single nanoshell, c) single roughened nanoshell, d) nanosphere pairs with interparticle axis perpendicular to the incident polarization, f) nanosphere pairs with axis parallel to the incident polarization, and g) nanoshell pair with axis parallel to the incident polarization [20].....32

Figure 2-10 The geometric effect of metal nanostructures under electromagnetic wave excitation [46]. 34

Figure 2-11 Cross-sectional $|E|^2$ profiles in different shapes of air nanogaps in 100 nm gold thin film. Strong electric field enhancement is observed due to focusing and coupling of the plasmons [17].....35

Figure 3-1 Top view of the nanosphere lithography. a) Deposition and self-assembly of polystyrene nanospheres on the substrate, b) Arrays of bowtie nanostructures after the metal deposition and removal of the nanosphere mask [51].....38

Figure 3-2 A schematic of the experimental setup. a) The microwave source, b) waveguide, c) illumination beam, d) dipole probe, e) bowtie structure. The total length L is 36 cm and gap size d is 1 cm. The incident electric field E is in the direction of the gap and magnetic field H is perpendicular to the gap [55].....40

Figure 3-3 a) Field intensity measured 2.5 cm in front of the open end of the rectangular waveguide without bowtie. b) Field intensity measured 0.5 cm behind the bowtie structure, which is positioned 2.5 cm in front of the waveguide. c) Intensity pattern of the measurements without bowtie (triangles), with bowtie along E- (squares) and H-directions (circles) [55]. 41

Figure 3-4 Layout of the bowtie geometry, where θ, t, d, and l are the gap angle, plate thickness, gap size, and tip width, respectively. E-line and H-line are along x-axis and y-axis in the gap area, respectively. 43

Figure 3-5 NEC 3D View of the waveguide from φ=55° and θ=55° polar coordinate angles. The 9 cm by 6 cm opening passes through the incident field towards the bowtie structure.....47

Figure 3-6 NEC 3D View from φ=270° and θ=60° polar coordinate angles. a) 3/8" thick single plate with 45° tip angle is modeled along X-axis with its tip at X=0 and Y=0 coordinates. b) The single plate is shifted in negative X-direction with half the size of desired bowtie gap size (1 cm). c) The bowtie structure that consists of the shifted original plate and its duplicate in YZ-plane, with 2 cm gap size.....48

Figure 3-7 Layout of the bowtie structures with 2 cm gap size and different tip angles. a) 45°, b) 90°, c) 135°, and d) 180° tip angles. 50

Figure 3-8 Layout of the 45° bowtie structure with 2 cm gap size expose by incident field through the 9 cm by 6 cm opening of the waveguide. 51

Figure 4-1 Layout of the 3/8" thick, 45° bowtie structure with 10 mm gap size. The electric field at the red dashed line along X-axis from -6 cm to 6 cm under the bowtie structure is calculated and analyzed. 53

Figure 4-2 The electric field simulation a) without, and b) with 3/8" thick, 90° bowtie with 10 mm gap size. The region of interest is a λ by λ area 5 mm under the bowtie. The bowtie focuses and enhances the electric field at the gap region. 54

Figure 4-3 a) The electric field simulation results with (solid line) and without (dashed line) 3/8" thick, 90° bowtie structure with 10 mm gap size. b) $|E_t|^2$ enhancement factor. X-axis goes from -6 cm (-0.5λ) to 6 cm (0.5λ). Bowtie gap is drawn to scale, but the rest of the structure is not.....55

Figure 4-4 a) NEC simulation, and b) experiment $|E_t|^2$ enhancement results of 3/8" thick 45°, 90°, 135°, and 180° bowties over varying gap size.....56

Figure 4-5 Examples of Self-Complementary Antennas [Public Domain Figure].....58

Figure 4-6 The effect of tip width change (from flat to sharp) on maximum electric field enhancement and optimal gap size. 60

Figure 4-7 The mode volume simulation based on electric field patterns in a) XY, b) XZ, and c) YZ planes. The electric field greater than 1/e (36%) of the maximum is shown. Red dashed box is the 2 x 3 x 3 cm^3 simulation region. 63

1. Introduction

1.1 Motivation

The ability to see matters with our own eyes allows us to discover and create new things. In my native language Mongolian, there is a saying that goes, "better see it once instead of hearing it a thousand times". From the beginning of time, people believed that the earth was flat because it looked flat from where they stood. There was no reason not to think so until Aristotle presented an argument in the 4th century BC based on the ever-changing round shadow of earth on moon [1]. Thus, the geocentric model of universe was proposed and believed for hundreds of years, which assumed that the spherical earth was in the center of the universe while the sun and other planets circled it around [2]. The father of observational astronomy Galileo Galilei invented an optical instrument in 1609 that allowed people to see outer space with their own eyes. The astronomical observations made possible by the telescope convinced people that the earth revolved around the sun [3]. Later in the 17th century, optical microscope was developed for observation of small objects, which advanced the study of life and living organisms significantly. Scientists were able to observe and influence how microorganisms and cells behaved, which led to the discovery of drugs that save millions of lives [4].

In the 21st century, studying the interactions of macromolecules such as DNA and RNA with other molecules and biomaterials helps discover their defects and develop new drugs to cure diseases. The conventional method to test how a certain molecule responds to drugs is to study how the entire population responds. However, it has been shown that averaging the signals of molecule population can be misleading [5] [6]. Individual molecules can exhibit different chemical and biological characteristics than the average

of the population. Single-molecule study techniques are free from inhomogeneity and ensemble averaging errors. Single-molecule detection (SMD) and analysis provide resolution that population measurement cannot [5]. Unfortunately, detecting a single molecule is a challenging task due to its physical size because the resolution of optical microscopy is limited by the laws of diffraction. Objects comparable to visual light wavelength (400-700 nm) in size cannot be imaged properly due to diffraction [7]. Therefore, single-molecule study requires advanced imaging techniques [8] [9].

1.2 Subwavelength Imaging Techniques

Single molecule imaging techniques are divided into two categories: optical- and force-based. Optical-based techniques include electron, fluorescence, and near-field microscopy. Force-based techniques consist of variety of scanning probe microscopies such as atomic force microscopy and chemical force microscopy. There are advantages and disadvantages to each of these microscopies [10].

Electron microscopy (EM) uses accelerated electrons as a source instead of light, and detects electrons that are transmitting, reflecting, or scattering from the sample. The resolution of electron microscopy has reached less than a nanometer, as the wavelength of electron is significantly shorter than that of visible light. However, EM is not compatible with biological samples because the sample under test gets electrically charged by high voltage electron gun. In addition, the sample must be in vacuum so that air molecules do not interfere with the electrons. EM is compatible with conductive nonbiological samples such as metal nanostructures and silicon-based MEMS [11].

Fluorescence microscopy uses light emitting properties of fluorescent chemical compounds by chemically attaching them to molecule under study. It is ideal for tracking the movement, monitoring the physical changes, and response to environment change [12]. However, optical signal from a single dye is very weak to distinguish from the background noise. The excited electrons of the fluorescent dye typically emit visual light. Large fluorescent dyes can hinder the molecules while small dyes are difficult detect due to diffraction limit. Fluorescence microscopy cannot account for structural changes and reactions with other molecules.

Scanning probe microscopy (SPM) uses physical probes with sharp tips to scan the sample surface. SPM can operate with the probe physically touching the surface (contact mode) or oscillating without touching (non-contact mode). The resolution can reach atomic level as the tip of the probe can interact and detect with individual atoms. It is suitable to investigate the surface of solid specimen. SPM is compatible for studying the force and extension of molecule bonds by attaching it to the surface and the tip, and retracting the probe away from the surface. However, SPM lacks chemical specificity and is not suitable for investigating time-dependent interaction between molecules and real-time detection [13].

1.3 Near-field Imaging

Near-field scanning optical microscopy (NSOM) surpasses the lower resolution boundary due to diffraction by detecting light at a distance much smaller than wavelength, i.e., before it diffracts. The light coming out of a molecule is detected before diffracting away from it. NSOM allows single-molecule detection as the resolution

becomes attainable. Raman spectroscopy is one of the most popular NSOM. In Raman spectroscopy, the sample is illuminated with laser beam and the reflection is collected by a lens through the aperture. The laser wavelength ranges from ultraviolet (10-380 nm) to near infrared (700-2500 nm). Depending on the characteristics of the small particles under excitement, energy of the laser collected by the lens is shifted from that of the illumination laser. The photons scattered from the sample can be either higher or lower energy than the incoming photons. Molecules are identified using Raman spectroscopy based on their unique vibrational information depending on their chemical bonds, known as a fingerprint of a molecule. It is also used for quantitatively mapping the individually identified particles based on many qualitative spectral information [14] [15] [16].

The scattering photons from the sample are called Stokes shifted if they have lower energy than the illuminated photons, anti-Stokes shifted if higher energy, and Rayleigh scattered if unchanged. Majority of the scattering photons simply reflect back without any energy change and are filtered out from the photons that contain critical information of the sample. The Stokes and anti-Stokes shifted photons typically have very low intensity as some of them are filtered along with the Rayleigh photons. Therefore, enhancement techniques have been developed to increase the sensitivity and resolution.

One of these techniques is called *surface-enhanced Raman spectroscopy (SERS)*. When a metal receives incident electric field, the free electrons accelerate and decelerate at the frequency of the incident field and generate electric field in all directions with lower amplitude due to loss. At the resonance frequency, called *plasma frequency*, the free electrons oscillate together in bulk with negligible loss, creating the plasmons. Due

to the lossless oscillation and incident field direction, plasmons of metal nanostructures generate localized and enhanced electric field. Raman spectroscopy utilizes this property of plasmons to enhance the electric field of incident laser without requiring a powerful laser. Metal nanostructures with nanometer-size gaps have shown high electric field enhancement inside the gap region due to the coupling of plasmons on either side. The resultant electric field is used for single molecule detection, as well as photodetection, subwavelength-resolution optical imaging, and single photon source [17] [19].

1.4 Objective of Thesis

The electric field enhancement generated by plasmons needs to be highest to boost Raman spectroscopy efficiently. The shape of the nanostructure heavily influences the enhancement factor. In particular, bowtie structures, two triangles placed in tip-to-tip configuration, have shown higher enhancement compared to other structures such as spheres and rectangles due to the plasmon collection at the tips [20].

Even in bowtie configuration, the electric field enhancement highly depends on the geometry of the structure. The geometry of the bowtie structure affects the coupling efficiency between the metals and incident field, and result in different enhancement amounts. Even though modern fabrication techniques such as focused-ion-beam, milling, and electron beam lithographies are able to produce nanostructures with gap size of few nanometers, fabricating the nanostructures with precise geometric variations to study their effects on electric field enhancement is challenging. However, the bowtie structures can be fabricated easily and their geometric effects can be studied in macroscale [17].

The purpose of this thesis is to determine the optimal geometry for maximum electric field enhancement in macroscale bowtie structures using radio frequency electromagnetic field source. The response of the electric field enhancement platform is simulated via the Numerical Electromagnetics Code (NEC-2). NEC-2 is a publicly available antenna-modeling program for electromagnetic analysis and response of antennas and metal structures. The bowtie structures with different tip angle, thickness, and gap size are modeled using antenna segments to determine the optimal design parameters for maximum electric field enhancement.

1.5 Thesis Outline

In Chapter 1, the purposes of imaging small objects and the common techniques are introduced. The objective of the thesis and how it is approached are briefly explained. Chapter 2 covers subwavelength imaging in detail. The techniques to improve biocompatible near field imaging by using plasmonic properties of metal nanostructures are discussed. Chapter 3 justifies the approach of this work via NEC-2 simulations. The way metal nanostructures and the excitation field in optical frequency are converted to macroscale model and radio frequency excitation field are described. In Chapter 4, the simulation results are presented. The optimal geometry parameters for maximum electric field enhancement are obtained from NEC-2. Finally, Chapter 5 concludes the thesis by summarizing the results and providing suggestions for future work.

2. Subwavelength Imaging and Plasmonics

2.1 Single Cell Imaging

Since the inception of time, humans have been discovering new things, traveling unexplored areas, and learning about nature. For every limitation to what we can do, a new technology and equipment were developed. With the invention of microscope in the 17^{th} century, the field of biology and medicine took a huge step towards discovering small organisms and their behaviors. Cell is the smallest unit of living organisms with individual biological properties. By visualizing cells under microscope, scientists were able to test drugs and find cures to diseases. Because biological studies typically investigate the behavior and response of large populations of cells to different environment and stimuli, the resulting signals must be averaged to find the response of that cell. However, the averaging of the cell population signals can be misleading due to inhomogeneity of the population [5] [6]. The signal of an individual cell is free of ensemble averaging errors and represents the true response of the cell [5]. Therefore, single cell biology is important to eliminate the errors and limitations of cell population studies.

The conventional optical microscope has high enough resolution to image a single cell, which typically has diameter of 1-100 μm. With immobilization and measurement techniques, biologists can capture cells with visual confirmation and test individually [21].

It is difficult to image living cells with bright-field microscope because they typically lack pigments that distinguish the features. Therefore, detection and imaging enhancement techniques have been developed for cell biology.

Fluorescent microscopy is a common technique that chemically labels the cells with fluorescent strains, which emit light upon excitation of the incident light. Based on the fluorescence emission, single cell detection is accomplished. Biological fluorescent strains are created to bind with and image the desired sample. Figure 2-1 shows the imaging of yeast cells without and with fluorescent tagging. Membrane proteins fused with fluorescent markers allow high definition of the membrane, which is difficult to distinguish. However, there are disadvantages in fluorescent strains such as phototoxicity, photobleaching, and invasiveness. The energy absorbed from light produces molecular changes that are toxic for the labeled cells. Due to the fading of the fluorescent effect of the strains, photobleaching, fluorescent microscopy cannot be used over extended period of time to study the cells. Finally, the strains reveal no specific information of the targeted cell, and can only be used for detection [22].

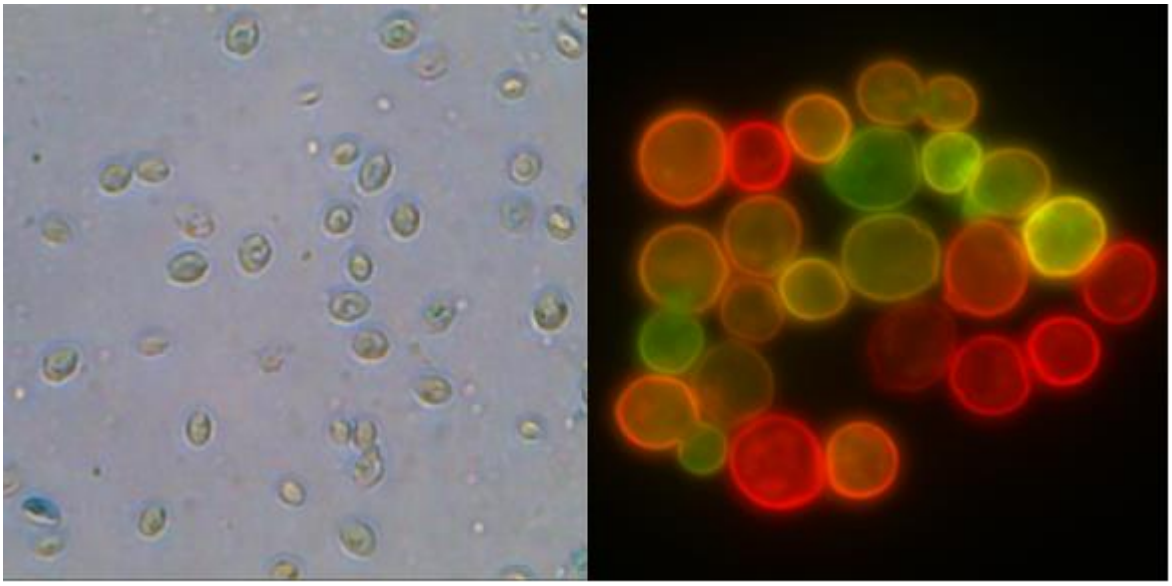

(a) *(b)*

Figure 2-1 a) Normal Yeast Cell under Conventional Optical Microscope, b) Yeast cell membrane visualized by membrane proteins fused with RFP and GFP fluorescent markers [Public Domain Figure].

Phase Contrast Microscopy is an optical microscopy technique that converts phase shift in light passing through the transparent specimen to brightness changes. The invisible phase shift becomes visible when converted to brightness variations. Permittivity is a material property that affects the Coulomb force between energy carrying electrons. When light travels through a medium with relative permittivity higher than 1 (vacuum), the amplitude and phase of the wave change due to the light and material interaction. The change in amplitude, due to scattering and absorption, is observed as brightness while the change in phase is invisible to human eyes. Phase contrast microscopy makes the phase change visible and thus reveals many transparent structures and features of cells. Other phase-imaging techniques have been developed for cell imaging [23] [24]. For example, Differential Interference Contrast microscopy

creates artificial shadow to enhance features of cells. Figure 2-2 shows the cell division process of yeast cells under phase contrast microscope.

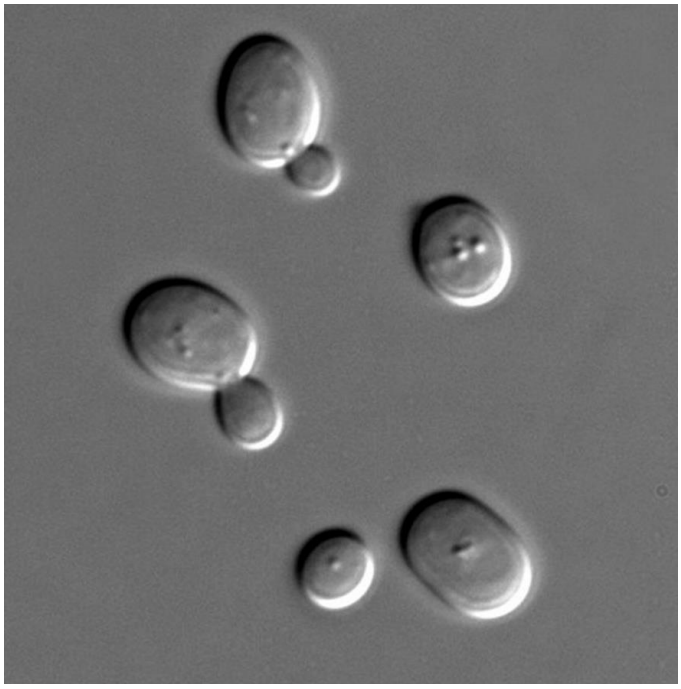

Figure 2-2 Phase Contrast Microscopy Image of Yeast Cell Division [Public Domain Figure].

Cells in human body are larger than a micrometer. Despite many challenges, cell study has significantly improved thanks to their convenient size. Because cells contain various organelles with multiple functionalities to survive, the overall size cannot be too small [25].

2.2 Single Molecule Imaging

The next level of biological structures and systems that defines life is *biomolecular complex*, a group of molecules such as protein, carbohydrates, DNA, and

RNA [26]. Properties of certain molecules are typically studied based on the reactions and interactions of the population of molecules. However, a single molecule study has been of interest since the 1990s because it provides high resolution and information that population measurement cannot. The highest resolution measurement that can be done in analytical chemistry is single molecule. Counting the solute molecules is the most accurate way to determine low concentrations. For example, benzene derivatives are studied at a *part per billion* (ppb) concentration. The maximum contaminant level for benzene in drinking water is set 5 ppb in the United States [27].

The quantitative information of molecular population can be misleading in many scenarios. The errors in transcription (DNA to RNA) and translation (RNA to protein) are averaged and contribute to the actual sequence analysis. Molecules with same primary sequence and molecular heterogeneity can result in different conformations and reaction rates. In these cases, single-molecule detection and analysis can provide full characterization of its behavior [28].

Furthermore, due to the high sensitivity and accuracy, single molecule detection (SMD) is of interest for detection of cell diseases, cancers, and genomic structural variants. Conventional genomic detection methods can give false results due to disadvantages like long experimental time, high cost, and contamination. In-solution and on-solid-surface optical SMD techniques have advanced biochemical and biophysical studies significantly [29].

2.3 Diffraction Limit

Although perfect for imaging small objects like cells, the previously mentioned optical microscopy techniques share one common limitation known as the diffraction limit. Due to the diffraction of light, optical microscope is unable to image objects as small as molecules.

In the 17th century, Dutch mathematician and scientist Christiaan Huygens proposed a theory about the way light travels as a wave. Huygens' principle suggests that every point on a wavefront of plane wave can be considered as a source of secondary spherical wavelet that travels in the forward direction at the speed of light. These infinitesimally small wavelets pulsate light in all directions at a specific frequency [30].

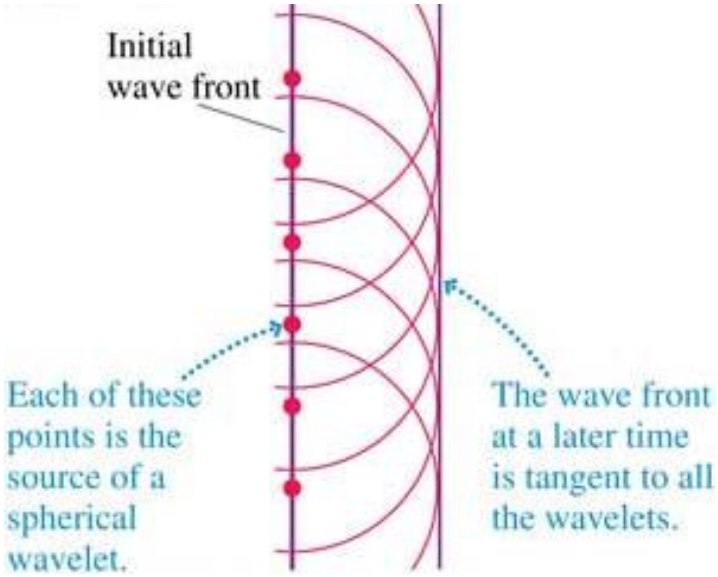

Figure 2-3 Plane Wave that Consists of Individual Hyegens' Wavelets Forming a Planar Wavefront [31].

When a plane wave of light meets an obstacle in its path, some of the wavelets are blocked while the unblocked wavelets continue traveling as a plane wave. The wavelet at the boundary of the obstacle, i.e. the diffraction point, acts as a point source and generates spherical wave, which can be expressed in three-space dimensions by [8]

$$\nabla^2 U + k^2 U = 0 \tag{1}$$

where

$$\nabla^2 U = \frac{1}{r^2}\frac{\partial}{\partial r}\left(r^2 \frac{\partial U}{\partial r}\right) + \frac{1}{r^2 sin\theta}\frac{\partial}{\partial \theta}\left(sin\theta \frac{\partial U}{\partial \theta}\right) + \frac{1}{r^2 sin^2\theta}\frac{\partial^2 U}{\partial \varphi^2} \tag{2}$$

where U is the amplitude of the wave at (r,θ,φ) spherical coordinates.

English polymath and physician Thomas Young experimentally showed the pattern of diffracted light using single- and double-slit screens. Young's experiment demonstrated two important phenomena for optical microscopy. Firstly, when the size of the single-slit becomes smaller, the pattern on the screen becomes wider and less focused (Figure 2-4). Secondly, the diffracted light rays from the double-slit creates constructive and destructive interferences (Figure 2-5).

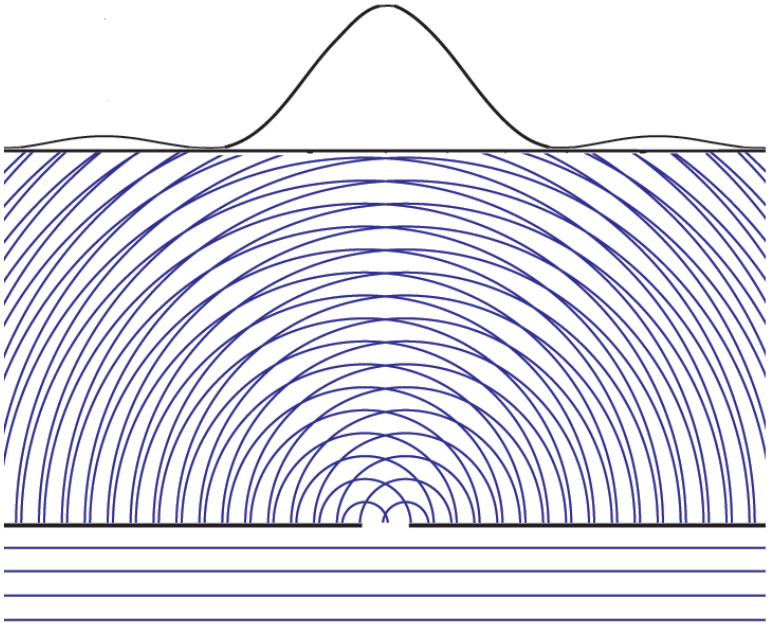

Figure 2-4 Single-Slit Diffraction Pattern [Public Domain Figure].

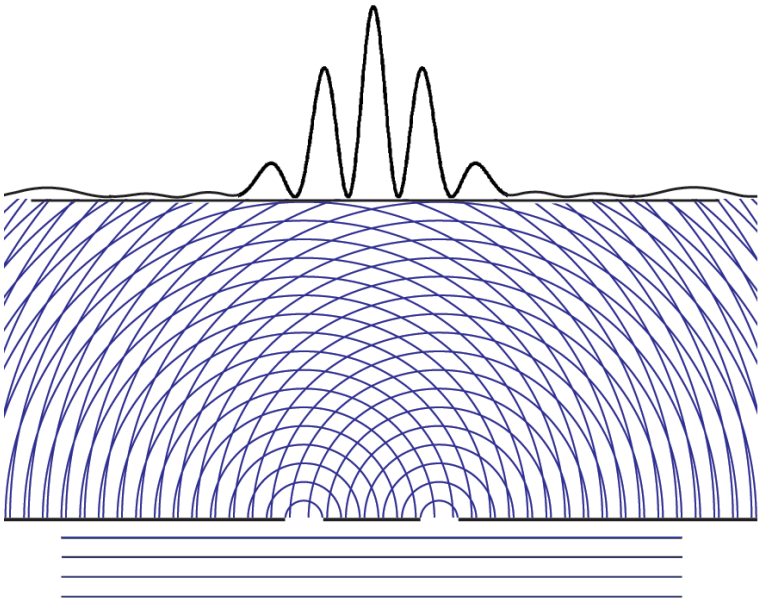

Figure 2-5 Double-Slit Constructive and Destructive Pattern [Public Domain Figure].

The propagation of far field light can be modeled by Fraunhofer diffraction equation (3) [32].

$$\mathrm{U}(x,y,z) \sim \iint_{-\infty}^{\infty} P(\xi,\eta) \cdot \mathrm{e}^{i\left(\frac{k}{2s'}\right)[\xi^2+\eta^2]} \cdot \mathrm{e}^{-i\left(\frac{k}{s'}\right)[x\xi+y\eta]} \cdot d\xi d\eta \qquad (3)$$

where k is momentum, s' is distance from the origin, ξ and η are Cartesian coordinates on the aperture plane, and P(ξ,η) is the pupil function, which is defined in absence of aberration and pupil absorption, as

$$P(\xi,\eta) = \begin{cases} 1 & inside\ the\ aperture \\ 0 & otherwise \end{cases} \qquad (4)$$

In optical microscopy, the objective lens captures the combination of reflected and diffracted light to image the object. When the object is large, the diffracted light is insignificant compared to the reflected light. On the other hand, when the object is small enough so that the diffracted light dominates, it is difficult to focus the small amount of scattered light optically (Young's single-slit experiment). When the diffracted rays are focused by the objective lens, the focused field distribution can be mathematically expressed by the Fourier transformation of the propagated field function.

The numerical aperture of the objective lens, the angle over which light can be accepted, plays an important role in focusing the diffracted light. The diffracted light rays focused by the objective lens produce a pattern of bright and dark rings, called an Airy disc, due to interference of the light rays with different phases (Young's double-slit experiment). The intensity distribution of the pattern focused by a circular objective lens was derived by Airy as:

$$\hat{I}(w) = C^2(\pi a^2)^2 \cdot \left[\frac{2J_1(2\pi aw)}{2\pi aw}\right]^2 \quad (5)$$

where *a* is aperture radius, *w* is distance from the origin, and $J_1(x)$ is Bessel function of order one.

The pattern of the focused light is a central bright spot surrounded by dark and bright concentric rings, known as Airy disc [7]. The radius of the bright spot is determined by the first minimum null, which occurs at $x=1.22\pi$. When two Airy discs are located nearby, the intensities overlap and the bright spots become indistinguishable.

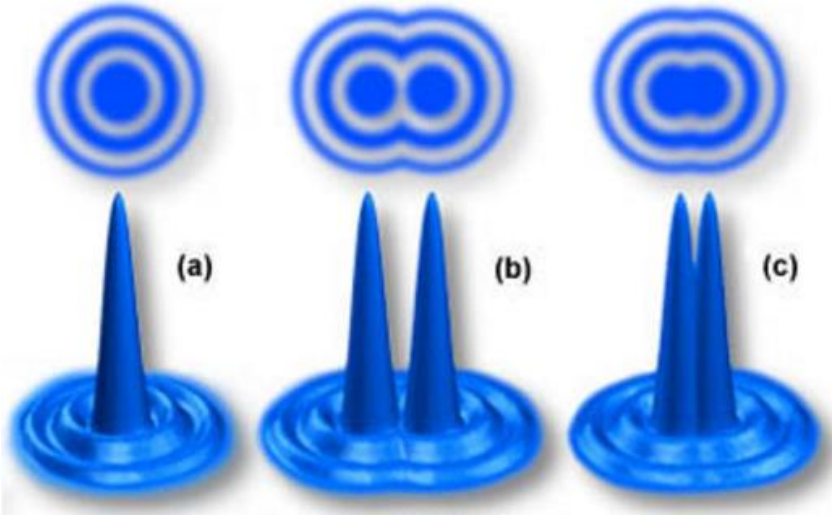

Figure 2-6 The intensity distributions of Airy discs. a) A single Airy disc, b) Non-overlapping Airy discs as a result of distinguishable objects, c) Overlapping Airy discs as a result of indistinguishably close objects [33].

The resolution of optical microscopy is defined by the minimum distance between two distinguishable, non-overlapping points as

$$r = \frac{1.22 \cdot \lambda}{2 \cdot NA} \quad (6)$$

where r is spot radius, λ is light wavelength, and NA is numerical aperture of the objective lens. The numerical aperture of the objective lens is defined by the refractive index of the medium n and half of the maximum angle θ of the cone of light that can enter the lens.

$$NA = n \cdot sin\theta \quad (7)$$

With the maximum numerical aperture of 1.3-1.4 for high magnification objective lenses, the highest resolution of the optical microscopy technique is limited by the laws of diffraction to image objects smaller than a few hundreds of nanometers. This includes viruses and molecules with typical sizes of 20-400 nm and less than 10 nm, respectively. To detect and investigate the properties of subwavelength objects like molecules, more advanced imaging techniques with higher resolution are developed [8] [9].

2.4 Near-Field Scanning Optical Microscopy (NSOM)

One of the subwavelength imaging techniques is near-field scanning optical microscopy. By investigating the features of a subwavelength size object at a distance much smaller than the incident light wavelength, the limitation posed by diffraction can be avoided. Instead, the resolution is limited by the size of the detector aperture. NSOM has achieved resolution less than a nanometer. Near-field imaging techniques are divided into two categories: force- and optical-based.

2.4.1 Force-Based Near-Field Imaging

The first force-based near-field imaging technique, scanning tunneling microscope (STM), was developed in 1981 at IBM. STM is based on the measurement of

quantum tunneling of electrons that travel from metal tip to sample surface or vice-versa when a voltage-biased probe with atomically sharp tip is brought near the sample. Precise control of the tip in all three dimensions is required to map the surface at high resolution. By measuring the electric current passing from the sample's atoms through the tip, the individual atoms are mapped. When the tip moves in XY-plane, the distance from the surface atoms and tunneling current change. There are *constant height* mode of operation based on the current changes, and *constant current* mode of operation based on the height change necessary to maintain constant current.

Based on STM, many other force-based scanning probe microscopies (SPM) are developed such as atomic, electrostatic, fluidic, and piezoresponse force microscopy. Similarly, SPM techniques use physical probes with sharp tips to scan the sample surface. SPM can operate with the probe physically touching the surface (contact mode) or oscillating without touching (non-contact mode). The resolution reaches atomic level as the tip of the probe can interact with and detect individual atoms. It is suitable to investigate the surface structure of solid specimen. However, SPM lacks chemical specificity that is crucial for biology and medicine. The main disadvantage of using SPM for biological applications like single molecule detection is the invasiveness of the probe that touches and interacts with free moving small objects.

2.4.2 Optical-Based Near-Field Imaging

A single molecule can be optically detected based on absorption, emission, scattering, and combination of light. Optical-based NSOM detects the non-propagating field from the object under study prior to diffraction. Because the intensity of this field

decreases exponentially with distance as it diffracts, the detector is placed as close as physically possible, only a few nanometers away from the object. Common optical-based NSOM techniques include Raman and fluorescence spectroscopy. Although subwavelength size objects like molecules can be detected using fluorescent nanoparticles that do not hinder the physical and biological activities of the molecules, the previously discussed disadvantages of fluorescence spectroscopy are incompatible with some applications. Raman spectroscopy is a label-free, non-invasive NSOM technique that provides the optical detection of molecules without the drawbacks of fluorescent. Raman spectroscopy is not interfered by water, which enables detection and study of aqueous based chemicals and biological samples. Compare to AFM, the Raman scattering experiments can be performed within seconds, allowing quick feedback of physical movement and interaction.

2.5 Raman Spectroscopy

Molecular spectroscopy studies the absorption of light by molecules. Molecules exhibit absorption depending on their chemical composition and energy states. The chemical combination of the atoms provides unique energy states and spectra of transitions between these states. The energy of a molecule consists of translational, electronic, rotational, and vibrational energies. The pattern of molecular energy is a unique characteristic that depends on the composition of the molecule. Recognition of the features of such pattern is enough to identify a molecule. Raman spectroscopy provides unique fingerprints of molecules based on the vibrational and rotational energy states. Molecular rotation gives rise to absorption in microwave and far infrared regions while molecular vibrations give rise to absorption in most of the infrared region. Furthermore,

the oscillating field of incident laser interacts with the molecules through their polarizability, which is determined by the electron cloud's ability to interact with electric field. Hard molecules with strong electric dipole moment such as water have weak Raman scattering while soft molecules such as benzene have strong Raman scattering [14] [15] [16].

In Raman spectroscopy, the sample under investigation is illuminated by a laser beam with wavelength ranging from ultraviolet to near-infrared. When the laser interacts with the sample, the photons are absorbed to excite the molecules to higher vibrational and rotational energy states. As the molecules relax back to lower energy states, the reemitted photons scatter with increased or decreased energy depending on the difference between the initial and final energy states ΔE_m. The amount of differential photon energy emitted or absorbed by the molecule is expressed as

$$\Delta E_m = E_p = hf \tag{8}$$

where h is Planck's constant (6.6256×10^{-34} joule·sec) and f is frequency. If the final energy state is higher, the molecule absorbs photons and gains ΔE_m energy. If the final energy state is lower, the molecule emits more photons and loses ΔE_m energy.

The electromagnetic absorption and emission of the sample are characterized by the wavenumber v. The wavenumber (cm^{-1}) is a number of waves in 1 cm long wave train.

$$v = \frac{\Delta E_m}{hc} = \frac{1}{\lambda} = \frac{f}{c} \tag{9}$$

where λ is wavelength, f is frequency, and c is speed of light ($2.99x10^{10}$ cm/s). The intensity of Raman scattering is quantified by the counts of detected photons per second. As this value depends on many apparatus-specific parameters, in most instances only relative intensities represent physically meaningful quantities. Thus, the Raman intensity scale is typically expressed in terms of arbitrary units or the scale is even omitted [6]. Given the characterization of a known sample, an unknown sample can be detected based on the comparison of the results. Figure 2-7 shows the Raman scattering of single layer carbon (graphene), multiple layers of carbon (graphite), suspended graphene, and graphene on substrate. Due to its unique electrical properties, graphene has become one of the popular materials of interest in 21st century [34]. The quality and property of graphene can be studied by the known Raman scattering of graphene, shown in Figure 2-7.

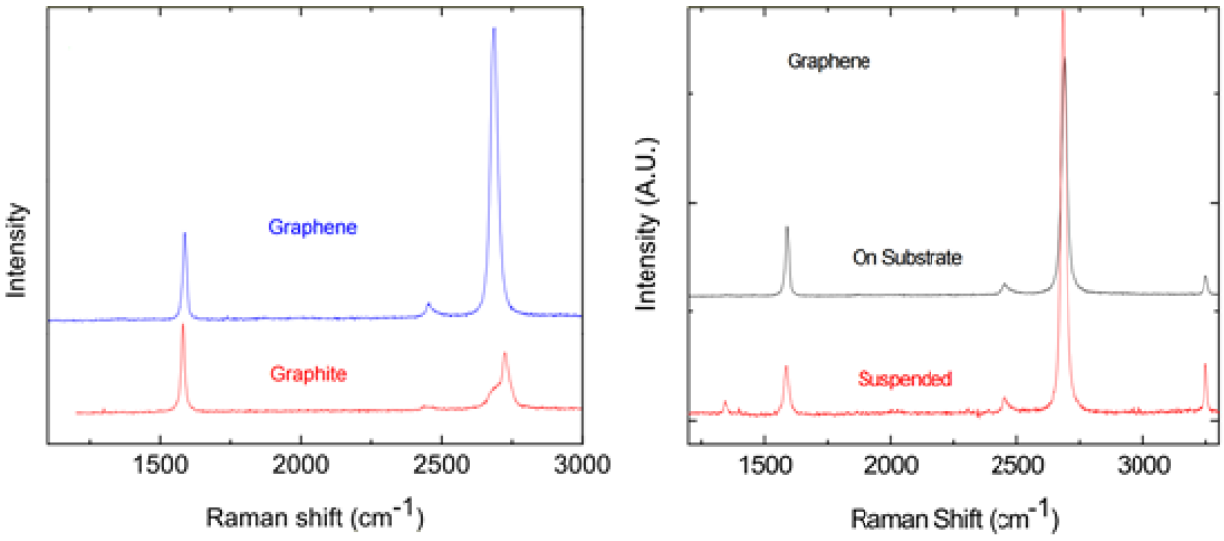

Figure 2-7 Raman Scattering of Graphene [35]. The intensity peaks allow one to distinguish the quality of graphene.

Table 2-1 shows the examples of Raman scattering frequencies of some organic compounds [18]. For instance, the asymmetric and symmetric vibrational stretches of nitro (R-NO2) group have distinguishable scattering frequencies, 1530-1600 cm^{-1} and 1310-1397 cm^{-1}. Vibrational frequencies of individual molecules have been studied and documented extensively.

Table 2-1: Examples of Raman Frequencies of some organic compounds [18].

Organic compounds	Frequency (cm^{-1})
Alkanes	
- CH_3 symmetric stretch	2862-2882
- C-C stretch	1040-1100
-Cyclopentane ring breathing	889
Alcohol O-H stretch	3635-3644
Acetylene C-H bend	825-640
Acetylene C≡C	2230-2237
C≡N stretch in R-CN	2230-2250
Cyanate C≡N	2245-2256
C-H in R-CHO	2800-2850
C=O in R-CHO	1730-1740
R-NO_2 asymmetric stretch	1530-1600
R-NO_2 symmetric stretch	1310-1397
C-S stretch	580-704
S-H stretch	2560-2590

Majority of the photons scatter with same energy (wavelength and frequency) as the incident photons because the molecules relax back to the initial energy state. This elastic scattering of incident photons is called Rayleigh scattering. Meanwhile, a fraction of the scattered photons (1 in 10 million) [5] have different energy because the final energy state is either higher or lower than the initial energy state. This inelastic scattering

of photons due to the interaction with matter is called Raman scattering. The photons are called Stokes shifted Raman scattering if the molecules relax to a lower energy state than their initial state and anti-Stokes shifted Raman scattering if they relax to a higher energy state.

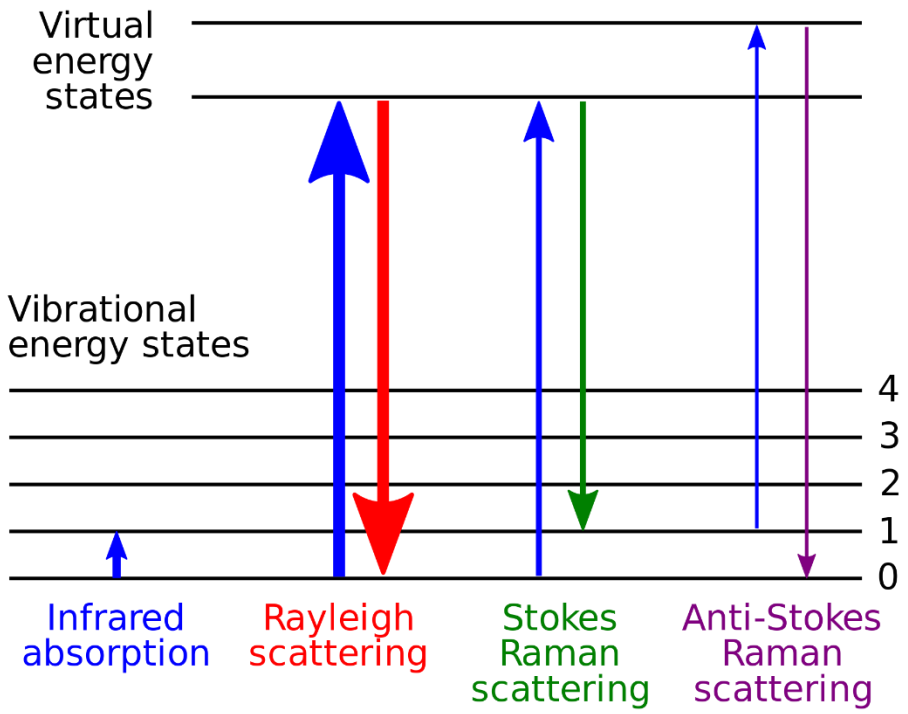

Figure 2-8 Raman spectra energy level diagram (Rayleigh, Stokes, anti-Stokes) [36].

Although Raman spectroscopy is a convenient, non-invasive tool to detect materials with high precision and accuracy, some disadvantages need to be improved. The Raman scattering effect is naturally very weak as only a few in millions of photons undergo Raman shift. Since the Rayleigh scattering of the photons reveal no information about the chemical composition, they are filtered out by variety of filters such as notch,

edge pass, or band pass filter [37]. The unfiltered Raman scattered photons that contain molecular information are collected by the detector, which can be too insignificant to detect. Therefore, Raman spectroscopy is improved by various methods for higher sensitivity and better detection.

2.5.1 Surface-Enhanced Raman Spectroscopy

One of the methods to improve the sensitivity of conventional Raman spectroscopy is Surface-Enhanced Raman Spectroscopy (SERS). Early investigations of Raman scattering of organic compounds on silver thin film has shown increase in intensity when the thin film was resonantly excited [19]. SERS received widespread attention when two research groups independently presented five to six orders of enhancement in 1977 [38] [39]. Silver films prepared by a variety of methods such as mechanically polished, photochemically roughened, and coldly evaporated have shown high enhancement [40] [41]. Upon further studies, it became evident that SERS is not limited to silver electrodes. Group 1b metals (gold, silver, and copper) and other specially prepared systems such as aluminum oxide evaporated on calcium fluoride film exhibited strong surface enhancement in early studies [36] [37]. The theory behind surface enhanced Raman scattering is extensively covered in many reviews.

The intensity of surface-enhanced Raman scattering can be expressed as

$$I_{Raman} \sim \omega_S^4 \cdot \left|\alpha_{eff}\right|^2 \cdot F^2 \cdot G_L \cdot G_S \qquad (10)$$

where ω_S is the Stokes frequency, α is a component of the Raman tensor that describes the polarizability of the molecule, and F is the electric field strength of the incident field. The additional G_L and G_S coefficients of SERS account for the magnification of electric

field at the site of the sample molecule and the Raman scattering. As the total enhancement factor varied greatly depending on the surface fabrication process, the understanding of the mechanism became important to maximize the enhancement.

Surface-Enhanced Raman Spectroscopy (SERS) utilizes plasmonic property of metals to localize and enhance the electric field and Raman scattering. To understand and optimize the surface enhancement, the plasmonic property of metal must be investigated.

2.6 Plasmons

When the free electrons of metals are excited with incident electromagnetic field, they oscillate at the frequency of the incident field. Because of the acceleration and deceleration during oscillation, electrons generate field with same frequency but lower amplitude due to the damping and loss. The Drude model of free electrons expresses the free electron oscillation as

$$m\frac{\partial^2 \boldsymbol{x}}{dt^2} + m\gamma\frac{d\boldsymbol{x}}{dt} = -e\boldsymbol{E} \tag{11}$$

$$\boldsymbol{x}(t) = \frac{e}{m(\omega^2 + j\gamma\omega)}\boldsymbol{E}(t) \tag{12}$$

where m is the mass of an electron, $\boldsymbol{x}$ is position, e is charge, $\boldsymbol{E}$ is incident electric field, ω is frequency of the incident field, and γ is damping or collisional frequency. In the absence of external charges and currents, Maxwell's equations that define how electric and magnetic fields interact with each other, surrounding charges, and currents in a medium can be written as

$$\nabla \times \boldsymbol{E} = -\frac{\partial B}{\partial t}, \quad \nabla \cdot \boldsymbol{E} = \frac{\rho}{\varepsilon_0} \tag{13}$$

$$\nabla \times \boldsymbol{B} = \mu_0 \left(\varepsilon_0 \frac{\partial \boldsymbol{E}}{\partial t} + \boldsymbol{j} \right), \quad \nabla \cdot \boldsymbol{B} = 0 \tag{14}$$

where $\boldsymbol{E}$ is the electric field, $\boldsymbol{B}$ is the magnetic induction, ρ is the induced internal charge density, $\boldsymbol{j}$ is the induced electric current density, ε_0 is permittivity, and μ_0 is permeability of free space. The induced charges and currents consist of the medium's response to the electromagnetic field, as a result of its polarization $\boldsymbol{P}$ and magnetization $\boldsymbol{M}$ [42].

$$\rho = -\nabla \cdot \boldsymbol{P} \tag{15}$$

$$\boldsymbol{j} = \frac{\partial \boldsymbol{P}}{\partial t} + c\, \nabla \times \boldsymbol{M} \tag{16}$$

Based on the polarization and magnetization fields, the electric displacement $\boldsymbol{D}$ and magnetic field $\boldsymbol{H}$ can be expressed as

$$\boldsymbol{D} = \boldsymbol{E} + 4\pi \boldsymbol{P} = \varepsilon \boldsymbol{E} \tag{17}$$

$$\boldsymbol{H} = \boldsymbol{B} - 4\pi \boldsymbol{M} = \frac{\boldsymbol{B}}{\mu} \tag{18}$$

The permittivity $\boldsymbol{\varepsilon}$ and permeability $\boldsymbol{\mu}$ determine a material's electromagnetic response to an incident field. Permittivity is a measure of how a propagating electric field is affected by the medium it is traveling through. It expresses how much electric field is generated per unit charge in the medium, i.e. the resistance of the medium. This response depends on the frequency of the incident field. The frequency dependent complex permittivity of a material is expressed by the Drude model as

$$\varepsilon_C(f) = 1 - \frac{f_P^2}{f(f + j\gamma)} = \frac{(f^2 + \gamma^2) - f_P^2}{f^2 + \gamma^2} + j \frac{\gamma}{f(f^2 + \gamma^2)} \tag{19}$$

$$Re\{\varepsilon_C(f)\} = \frac{(f^2 + \gamma^2) - f_P^2}{f^2 + \gamma^2} \tag{20}$$

where f_P is plasma frequency, γ is damping or collisional frequency, and f is incident field frequency.

When the frequency of the incident field surpasses the plasma frequency of that material, electrons can no longer keep up with the incident field and let it pass through without interaction. Most metals are transparent to x-rays and gamma rays because their plasma frequencies are in the ultraviolet range. The plasma frequency of a metal depends on the density of electrons and is expressed as

$$f_P = \frac{1}{2\pi}\sqrt{\frac{n_e \cdot e^2}{m \cdot \varepsilon_0}} \tag{21}$$

where n_e is the density of electrons, e is the electric charge, m is the effective mass of the electron, and ε_0 is the permittivity of free space (F/m). At the plasmon resonance condition (plasma frequency), the free electrons bundle with high Coulomb's interaction, absorb the incident field completely, and oscillate together in bulk with little to no loss.

2.6.1 Localized Surface Plasmons

When the frequency of incident field is near plasma frequency, metal structure with dimensions smaller than the incident light wavelength demonstrated high absorption of incident electromagnetic field and localized electric field generation. The collective free electrons of the metal nanostructure that couple with the incident field are called the *localized surface plasmons*. The electric field is amplified near the metal nanostructure due

to the localized plasmon resonance. The surface of the metal applies an effective restoring force on the plasmons and creates resonance.

The localized surface plasmons highly depend on the size of the metal structure. For metal nanoparticles much smaller than the wavelength of light, the electron oscillation is considered to be dipolar. The collective oscillation of the free electrons can then be described by the dipolar polarizability α as [43]

$$\alpha = (1 + k)\varepsilon_0 V \frac{(\varepsilon_C - \varepsilon_m)}{(\varepsilon_C + k\varepsilon_m)} \tag{22}$$

where V is volume of the nanoparticle, ε_m is the permittivity of the medium, and k is shape factor that defines the dependence of polarizability on geometry of the surface. The resonance condition is satisfied when the polarizability becomes maximum, i.e. when the denominator is zero.

$$\varepsilon_C + k\varepsilon_m = 0 \tag{23}$$

$$Re\{\varepsilon_C\} = -k\varepsilon_m \tag{24}$$

Substituting the real part of the complex permittivity expressed in (19) while assuming the collision frequency is negligible, the localized surface plasmonic resonance (LSPR) frequency can be written as

$$f_{SP} = \frac{f_P}{\sqrt{1 + k\varepsilon_m}} \tag{25}$$

It can be seen that the LSPR frequency depends on the shape of the nanoparticle and the permittivity of the medium. LSPR frequency shift of fixed nanoparticles can be used to detect changes in the medium.

Table 2-2 shows the plasma frequencies of metals commonly used in LSPR applications. Given that the plasma frequency is typically in ultraviolet range, the surface plasmonic resonance frequency will fall within the optical or infrared range depending on the shape and medium. The visual observability and biocompatibility make them ideal for various applications such as biosensing, localized hyperthermia, and more.

Table 2-2 Plasma frequencies and wavelengths of metals commonly used for LSPR applications [44]

Metal	Plasma Frequency (PHz)	Plasma Wavelength (nm)	Spectrum
Gold	2.18	137.43	Far Ultraviolet
Platinum	1.24	241.16	Middle Ultraviolet
Silver	2.18	137.61	Far Ultraviolet
Aluminum	3.57	84.03	Vacuum Ultraviolet

The LSPR oscillation generates enhanced electric field localized near the surface of the nanoparticles, which can be expressed as [43]

$$E_{SP} = \frac{(1+k)\varepsilon_m}{(\varepsilon_c + k\varepsilon_m)} E_0 \qquad (26)$$

At the resonance frequency, the localized electric field is very high due to the LSPR. Because the intensity of the incident field is proportional to the square of the electric field, the *enhancement factor* due to the LSPR or charge focusing will be denoted as $|E_t|^2$ for the rest of the thesis.

$$|E_t|^2 = \frac{|E_{SP}|^2}{|E_0|^2} \quad (27)$$

In Surface-Enhanced Raman Spectroscopy, the incident field is enhanced by a factor of $|E_t|^2$. Upon interactions with the sample molecules, the Raman scattered photons in near-field of the metal nanoparticles are enhanced by a factor of $|E_t|^2$ as well. Therefore, the overall enhancement in SERS due to LSPR is $|E_t|^4$. SERS has demonstrated a total enhancement factor of 10^{14}-10^{15} [45].

2.6.2 Coupling of Localized Surface Plasmons

When two metal nanoparticles are brought nearby, each nanoparticle interacts with the combination of the incident field and the enhanced field of the other nanoparticle. The plasmonic coupling of nanoparticles result in even stronger localization and higher enhancement than a single nanoparticle. The enhancement factor depends on the amount of electric field due to individual nanoparticles and physical positioning of the coupling nanoparticles. Figure 2-9 shows the Finite-Difference Time-Domain (FDTD) simulation results of electric field enhancement in gold nanospheres and nanoshells. Individually, the nanoshell exhibited stronger enhancement than the nanosphere due to the distribution of holes (Figure 2-9 (a) and (b)) [20].

The coupling of the plasmons occurs when the interparticle axis of the nanoparticles is parallel to the incident electric field polarization. Figure 2-9 (d) and (e) show little to no coupling between the pairs of nanoparticles (dimer) when the incident polarization is in Y-axis while the nanoparticles are aligned in X-axis. On the other hand,

when the incident polarization is parallel, the electric fiend enhancement is up to 100 times.

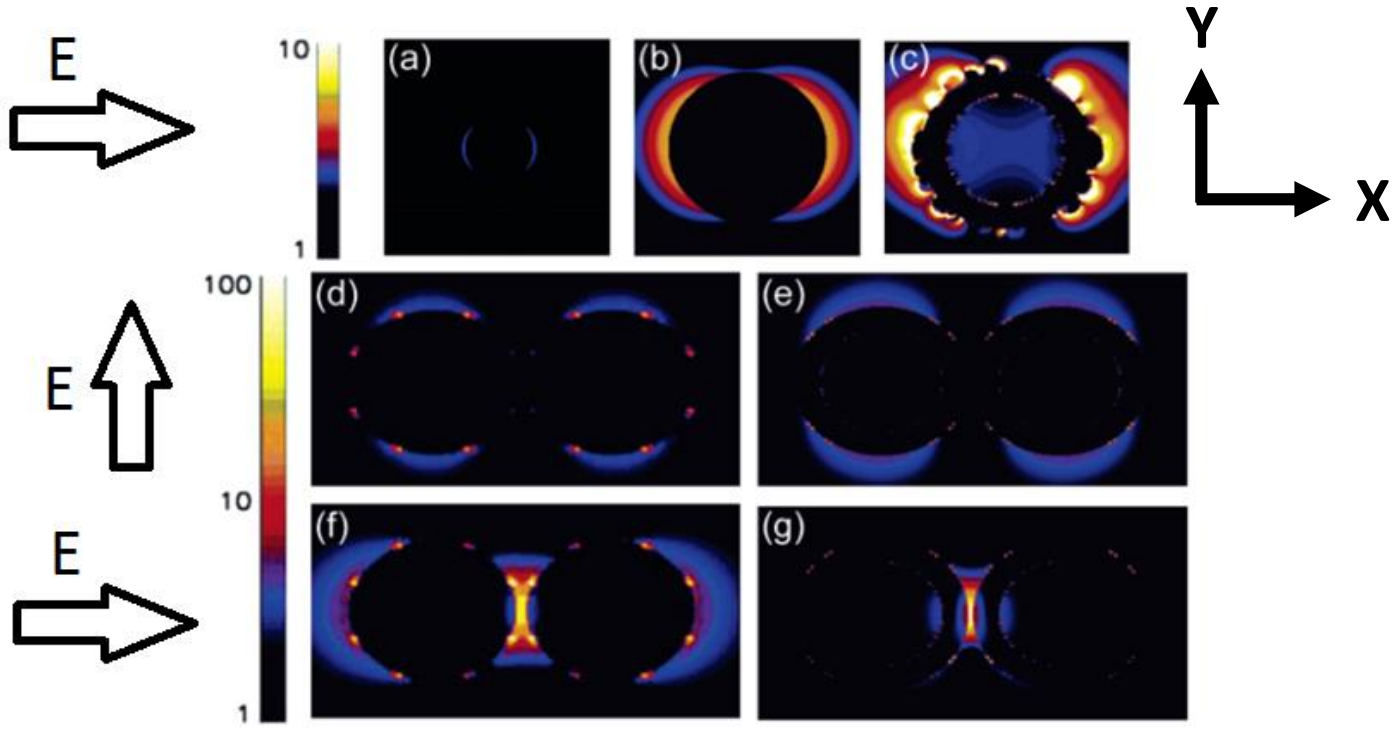

Figure 2-9 Detailed view of the effect of physical location on the electromagnetic field enhancement |E| in gold nanoparticles. a) Single nanosphere, b) single nanoshell, c) single roughened nanoshell, d) nanosphere pair with interparticle axis perpendicular to the incident polarization, e) nanoshell pair with interparticle axis perpendicular to the incident polarization, f) nanosphere pairs with axis parallel to the incident polarization, and g) nanoshell pair with axis parallel to the incident polarization [20].

Table 2-3 Electric field enhancement factors for gold nanospheres and nanoshells in different configurations [20]

Excited Particles	**|E|**	**$\|E\|^4$**
Individual Nanosphere	2.7	53
Nanosphere Dimer (⊥)	4	256
Nanosphere Dimer (||)	43	$3.4x10^6$
Individual Nanoshell	6.1	1385
Roughened Nanoshell	14	$3.8x10^4$
Nanoshell Dimer (⊥)	5	625
Nanoshell Dimer (||)	85	$5.2x10^7$

Figure 2-10 shows metal nanosphere and nanotriangle under electromagnetic wave excitation. Due to the shape of the structure, the charge density and electric field localization at the tip of the nanotriangle are higher. The roughened nanoshell in Figure 2-9 (c) exhibits higher enhancement than the smooth nanoshell due to the surface roughness as well. The close placement of sharp tips with focused plasmonics has shown higher enhancement factor than smooth nanoparticles.

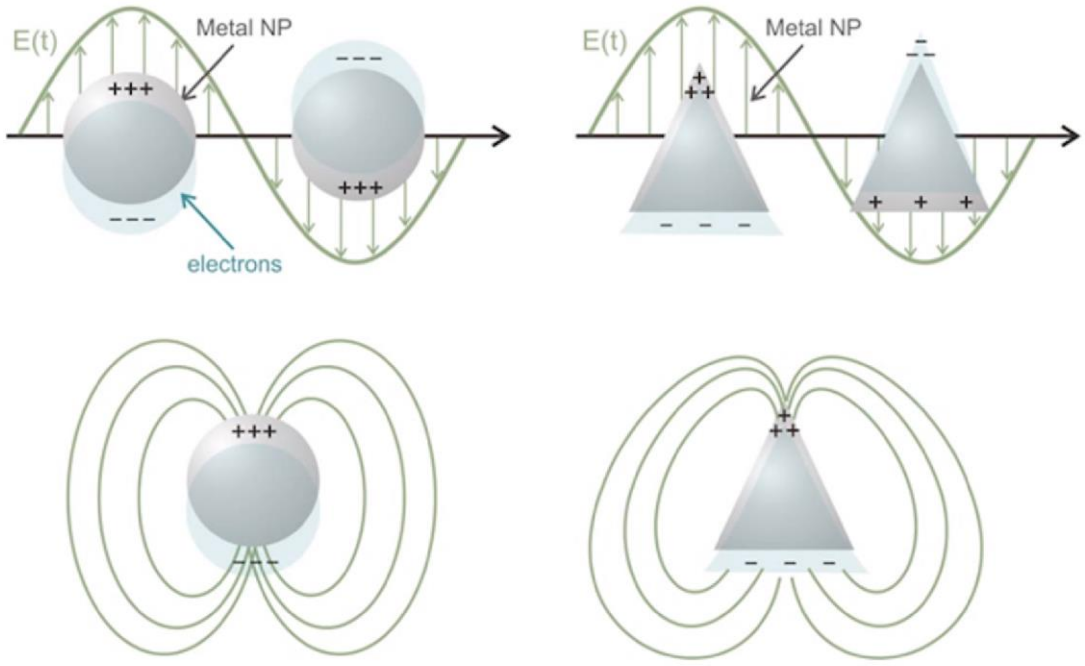

Figure 2-10 The geometric effect of metal nanostructures under electromagnetic wave excitation [46].

Myung-Ki Kim *et al*. has demonstrated the shape dependency of plasmonic focusing and distance dependency of plasmonic coupling [17]. Bowtie shaped tip-to-tip triangular gold nanostructures with air nanogap are fabricated by focused ion-beam (FIB) milling techniques. Figure 2-11 shows the electric field enhancement due to the focusing and coupling near the nanogap. The first two nanostructures exhibit very little focusing and almost no coupling because the tips are not sharp and too far apart. Meanwhile, the plasmons in the last two bowtie structures are highly focused and coupled, and the electric field enhancement is several orders higher. The sharp gold bowtie structure (Figure 2-11d) with g = 5 nm air gap has demonstrated $|E|^2$ enhancement factor of 400,000, which is two orders higher than that in nanoshell dimer in Figure 2-9.

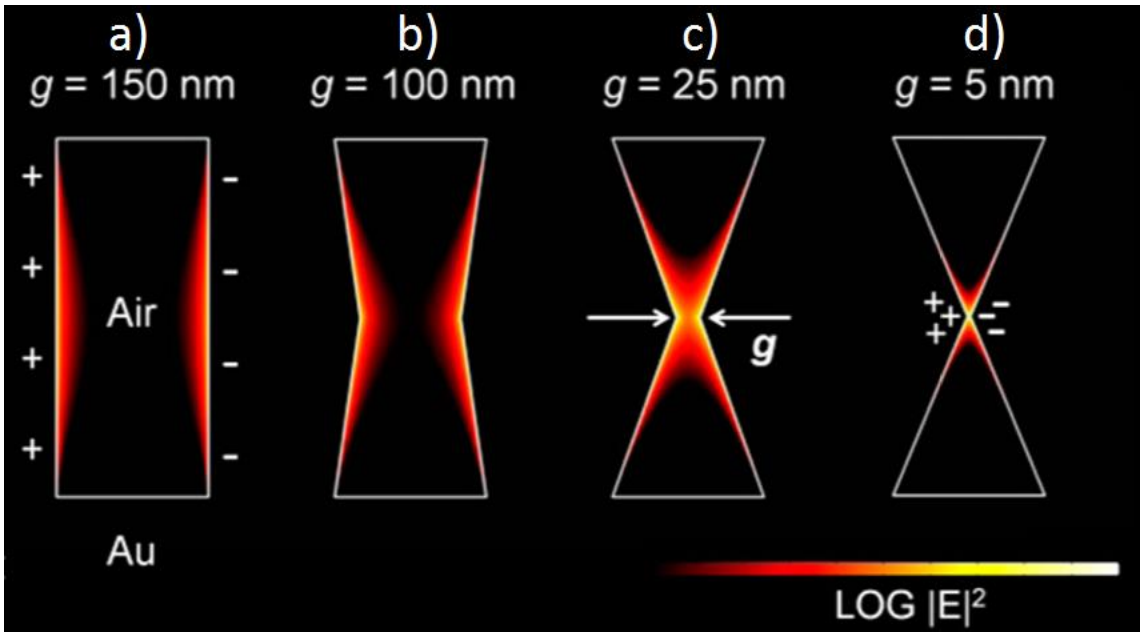

Figure 2-11 Cross-sectional $|E|^2$ profiles in different shapes of air nanogaps in 100 nm gold thin film. Strong electric field enhancement is observed due to focusing and coupling of the plasmons [17].

The enhancement factor variation is further explained by the *mode volume,* a region where the plasmons are focused and strong electric field enhancement is observed. Mode volume is a dimensionless unit in terms of the cubit wavelength (λ^3). The combination of the enhancement factor and mode volume is observed to be constant for the bowtie structures with different tip angles.

$$V_{mode} = \frac{Volume\ (m^3)}{\lambda^3\ (m^3)} \tag{28}$$

$$V_{mode} \cdot |E|^2 \approx 0.1 \tag{29}$$

The relationship between the mode volume and enhancement factor is a representation of the plasmon focusing: the more focused the plasmons are in a small volume, the more the

enhancement factor is. In addition to the nanoparticle sharpness, the distance between the coupling nanoparticles is an important parameter for the mode volume.

2.7 Optimization of Electric Field Enhancement

To benefit Raman spectroscopy and other applications, the electric field enhancement property of LSPR must be utilized to its fullest potential. A number of parameters that affect the enhancement factor is discussed in this section. Firstly, the size of the nanoparticles must be smaller than the incident wavelength so that the collective oscillation of the free electrons is dipolar. Secondly, the shape of the nanoparticles must be optimized to focus the maximum amount of plasmons in a small region. Lastly, the gap between the nanoparticles must be optimized for maximum coupling between the plasmons. The minimization of the mode volume is of importance to obtain the highest enhancement factor as well.

Many studies of enhancement factor have been done by fabricating metal nanoparticles and measuring it. However, it is very challenging to fabricate nanoparticles with precise incremental difference in the geometry dimensions to find the optimal condition. Chapter 3 will discuss the approach to find the optimal geometry for maximum enhancement factor in depth.

3. Macroscale Experiment and NEC Modeling

3.1 Difficulties in Nanoparticle Fabrication

Detection of low concentration contaminants (<100 ppb) and single molecule characterization have been demonstrated by various utilizations of surface enhanced Raman spectroscopy and metal nanostructures [46] [47] [48]. However, it has been a challenging task to obtain the highest possible enhancement. As covered in Chapter 2, the enhancement factor depends on the shape of the nanoparticles. C. J. Orendorff *et al*. studied gold nanoparticles with various shapes such as sphere, rods with different aspect ratios, dogbones, etc. The shape dependent enhancement factor varied by a factor of 10^2 [49]. In other previously cited studies, a pair of triangular nanoparticles in shape of a bowtie demonstrated higher enhancement factor than those in different shapes. Further studies could be done to fully understand the effects of geometric parameters and maximize the enhancement factor.

The common techniques to fabricate nanoparticles are focused ion beam (FIB) lithography, electron beam (e-beam) lithography, and nanosphere lithography (NSL). However, the fabrication of nanoparticles with incremental variations of the geometric dimensions and angles is challenging. Most nanolithography techniques require expensive equipment, complicated process, and other issues [50]. NSL is a popular, low-cost technique to fabricate homogenous arrays of nanoparticles with different sizes. This wafer-level nanoparticle fabrication technique benefited the plasmonic coupling and electric field enhancement studies.

A flat substrate is coated with an organized layer of polystyrene micro/nano-spheres by evaporation or natural self-assembly process (Figure 3-1 (a)). This layer of nanospheres is used as a mask to deposit metal on the exposed parts of the substrate (Figure 3-1 (b)). The mask is removed by a solvent (lift-off process) along with the unnecessary metal.

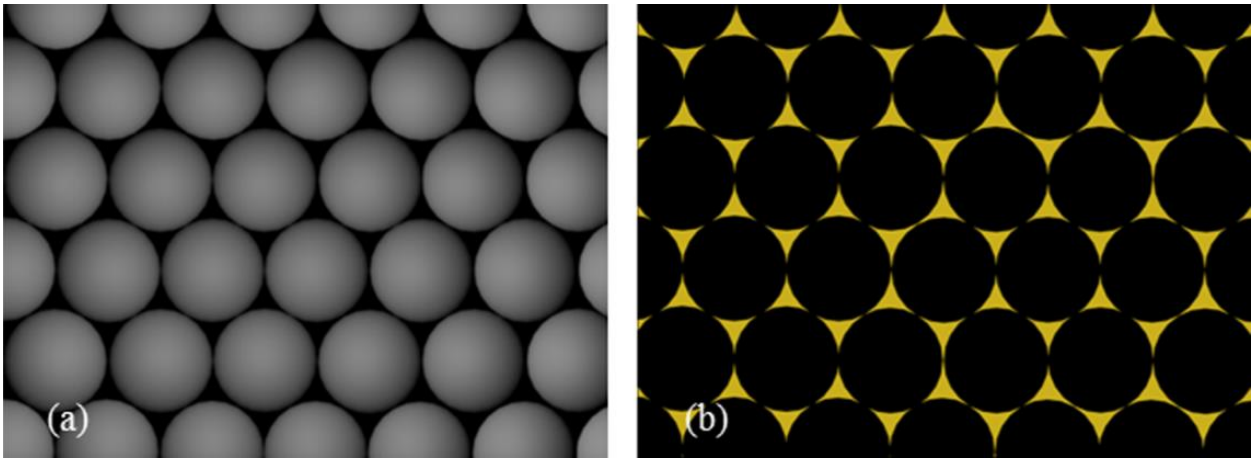

Figure 3-1 Top view of the nanosphere lithography. a) Deposition and self-assembly of polystyrene nanospheres on the substrate, b) Arrays of bowtie nanostructures after the metal deposition and removal of the nanosphere mask [51].

The size and shape of the bowtie nanostructures fabricated by NSL have been modified and tuned by new approaches. Depositing a secondary layer of nanospheres or tilting the substrate during metal deposition allows controlling the size, shape, and interparticle spacing to be controlled [52] [53]. However, the tip angle of individual triangle and gap size of the bowtie have upper and lower limits, respectively, because they are determined by the radius and shape of the spheres.

Besides the fabrication challenges, the nanoparticles have exhibited other problems that limited the high electric field enhancement. In some studies of nanoparticles bonded with chemicals, the ratio of enhancement factors in SERS and normal Raman ($|E_{SERS}|^2/|E_{Raman}|^2$) has been less than 1 order of magnitude [54]. In other studies, the success rate of efficient or "hot" nanoparticles that enhanced the electric field has been as low as 1 out of 100 to 1000 nanoparticles [47]. These inconsistencies complicate the study of the geometric effects on electric field enhancement.

3.2 Macroscale Enhancement Experiment

One of the reasons why electric field enhancement depends on geometry of the individual structure is charge focusing. The localized accumulation of electrons depends on the shape of the structure under incident field excitation. Even though the localized surface plasmonic resonance may not occur, the geometry dependent charge focusing can be studied using macroscale metal structures. At macroscale, the parameters can easily be modified. Unlike nanoparticles, the macroscale structures can be designed with precise control over the geometry.

The incident field wavelength is of importance for macroscale experimental results to be applicable in nanoscale applications. The metal nanoparticles are typically smaller than the wavelength in nanoscale for previous studies. Therefore, the incident field must be in the radio frequency range with wavelength in an order of meter, depending on the size of the macroscale structure.

3.3 Previous Work

The proof-of-principle measurements in macroscale have been presented by R.D. Grober *et al*. in 1997 [55]. The localization and enhancement of incident field in a metal bowtie structure was experimentally studied by exciting the bowtie by electromagnetic wave and measuring the radiated power. The incident 2.2 GHz microwave source is directed by a rectangular waveguide towards the bowtie gap, as shown in Figure 3-2. The gap is 2.5 cm away from the waveguide. The bowtie structure consists of two 1-cm-thick aluminum triangular plates with 90° tip angle and 17.5 cm height (Figure 3-2). The radiated power is measured by a dipole probe located 0.5 cm behind the bowtie.

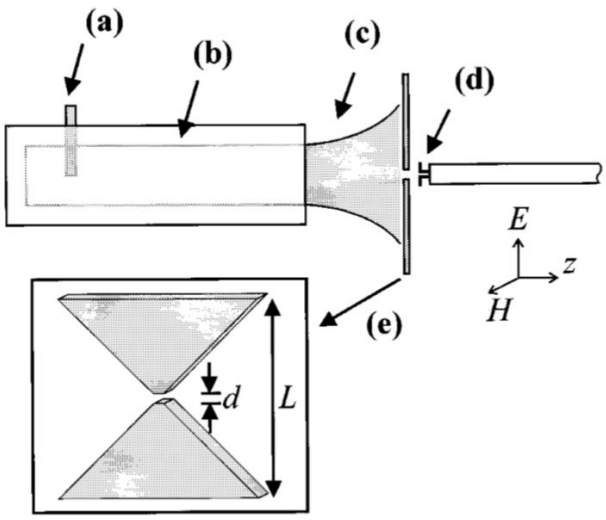

Figure 3-2 A schematic of the experimental setup. a) The microwave source, b) waveguide, c) illumination beam, d) dipole probe, e) bowtie structure. The total length L is 36 cm and gap size d is 1 cm. The incident electric field E is in the direction of the gap and magnetic field H is perpendicular to the gap [55].

To compare the effect of the bowtie, the radiated power is measured with and without the bowtie in between the waveguide and dipole probe. Figure 3-3a shows the

measured profile of the radiation as a Gaussian with λ/2 diameter (λ=13.6 cm) when the dipole probe is 2.5 cm away from the waveguide. Figure 3-3b shows the localized and enhanced intensity in presence of the bowtie, which is located 2.5 cm from the waveguide and 0.5 cm from the dipole probe. The uneven localization of the intensity is shown in Figure 3-3c, where the intensity in H-direction has lower Q factor. The presence of the bowtie focused the radiated power significantly and enhanced by 30%.

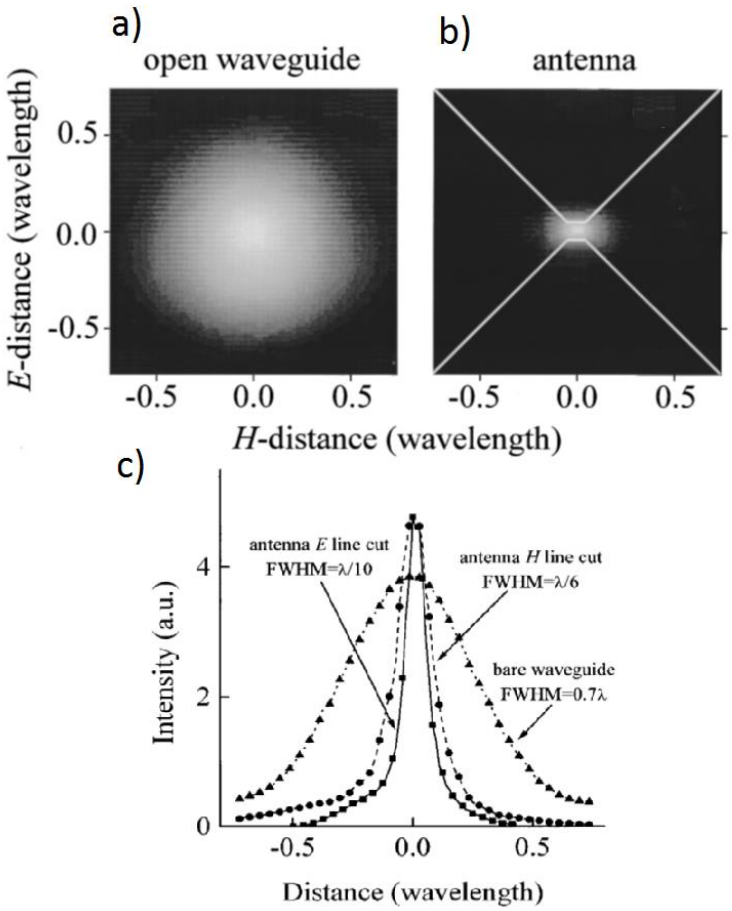

Figure 3-3 a) Field intensity measured 2.5 cm in front of the open end of the rectangular waveguide without bowtie. b) Field intensity measured 0.5 cm behind the bowtie structure, which is positioned 2.5 cm in front of the waveguide. c) Intensity pattern of the measurements without bowtie (triangles), with bowtie along E- (squares) and H-directions (circles) [55].

Even though this study has experimentally shown that macroscale metal bowtie can be used to localize and enhance incident electromagnetic field, there are several inconsistencies that need to be addressed. First, the distance between the waveguide and dipole probe is different between the two experiments. Without bowtie, the dipole probe is 2.5 cm away from the waveguide. With the 1 cm thick bowtie, which is 2.5 cm from the waveguide, the probe is 0.5 cm away from the bowtie, making the total distance between the probe and waveguide 4 cm. To measure the actual effect of bowtie, the intensity of the electromagnetic field should be measured at the same location. Since the intensity decays over distance, the intensity at 4 cm from the waveguide could be much smaller than at 2.5 cm. Thus, the actual enhancement factor could be higher than 30%.

Secondly, the wavelength of the incident field (13.6 cm) is smaller than the bowtie structure (17.5 cm height, 35 cm base), which conflicts with nanoscale studies. As shown in Figure 3-2, although the rectangular waveguide limits the incident field to a certain region, the exposed part of the bowtie appears to be larger than the wavelength. In fact, no information about the size of the waveguide is provided in this paper. To stay consistent with the nanoscale studies, the bowtie structure should be smaller than the wavelength or the exposed portion limited by a waveguide smaller than the wavelength. Since the metal plates can be designed and modified easily in macroscale, structures with different geometry parameters should be studied extensively to find the optimal conditions for maximum electric field enhancement.

3.4 Approach of the Thesis

In our previous work [56], the electric field enhancement in macroscale aluminum bowtie structure is studied by experiment and simulation. The objective is to find the optimal geometry parameters that maximize the enhancement. The simulation supplements the experiment by designing the elements similarly and performing simulations under same conditions. This thesis focuses on the simulation portion of the "optimization of the bowtie gap geometry for a maximum electric field enhancement". The simulations are performed in Microwave Laboratory at Marquette University. This work exploits the previous study of macroscale bowtie by varying the geometry parameters: gap angle (θ), plate thickness (*t*), gap size (*d*), and tip width (*l*). Figure 3-4 and Table 3-1 show the geometry parameters and their variations. The experiment and simulation are performed at 2.45 GHz (λ=12.2 cm) in RF range.

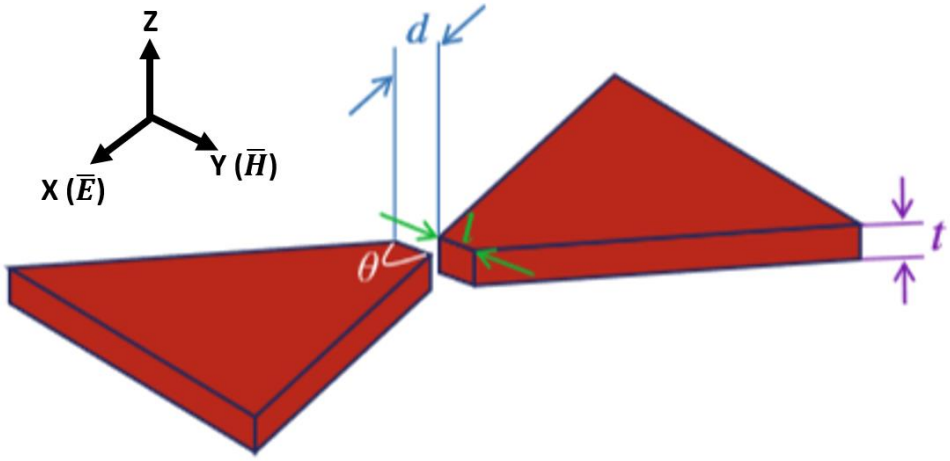

Figure 3-4 Layout of the bowtie geometry, where θ, t, d, and l are the gap angle, plate thickness, gap size, and tip width, respectively. E-line and H-line are along x-axis and y-axis in the gap area, respectively.

Table 3-1 Variant geometry parameters of the bowtie

Parameters	Angle (θ)	Thickness (*t*)	Gap size (*d*)
Range	45°	1/8”	0-0.5 λ
	90°	1/4”	
	135°	3/8”	
	180°		

The response of the electric field enhancement platform is simulated by the Numerical Electromagnetics Code (NEC). NEC is a publicly available antenna-modeling program for electromagnetic analysis and response of antennas and metal structures. It uses the electric field integral equation for thin wires and magnetic field integral equation for closed surfaces to iteratively calculate the currents and electric field. NEC can be used to model various antenna-based platforms to study their electromagnetic responses [57] [58]. There are various input cards that activate and control the features of the software. The full extent of the program description and operation can be found in the original NEC document and other technical manuals [59] [60]. there are guidelines for modeling wire structures in NEC. A few of the modeling rules that limit the design of our simulation platform include:

- The length of an antenna segment should be greater than 0.001λ and less than 0.1λ

Since the wavelength λ is 12.2 cm, the segment length is typically 1-1.2 cm to build large structures that comply with the NEC rule. Wires longer than 1.22 cm are broken into multiple segments shorter than 1.22 cm.

- The radius of a segment should be less than 1/8 of its length

The radius of all segments is chosen as 0.5 mm, which dictates the lower boundary of the segment length at 4 mm. This rule is satisfied as the shortest length of a segment used in this thesis is 6 mm.

- The circumference of a segment should be much less than λ (12.2 cm)

The circumference of a circle with 0.5 mm radius is 3.14 mm, which is 2.5% of the wavelength.

All geometric and structural rules are met based on the wavelength of the incident field. The “segment check” and “geometry check” features of NEC validate the input code for all requirements and errors of the software for most precise and efficient simulation.

Since the length and radius of a segment are limited by the wavelength, the number of segments determines the size of a platform that can be modeled by NEC. Some versions of NEC can support models with up to 11000 segments depending on the computer RAM. The computer used for this thesis is capable of supporting 8000-segment simulations, which prohibits fine wiring of the platform. To cover large areas, 1.2-2.4 cm long wires are used and broken into 2 segments with 0.6-1.2 cm length to satisfy the rule.

3.5 Modeling of the Experimental Components

Our experimental setup consists of a transmitter monopole antenna, 9 cm by 6 cm rectangular waveguide, bowtie structures, and receiver antenna. The simulation frequency is chosen as 2.45 GHz to match the experiment because the transmitter and receiver antennas have the lowest reflection and highest transmission at 2.45 GHz. All experimental elements are modeled in NEC by segments.

Transmitter antenna is modeled by five 6 mm long segments with a total length of 3 cm. A voltage source is applied by the Excitation (EX) card at the middle segment to radiate electromagnetic field. The transmitter antenna is positioned along X-axis and 2 meters (>10λ) above the rest of the platform so that the electric field is in X-axis direction and far field.

Receiver antenna of the experiment is not modeled because NEC has a built-in single-point detector that can scan the region of interest and calculate the near electric fields in the vicinity. The Near Fields (NE) card allows users to program the region of interest with higher precision and freedom than physical antennas in experiment.

Waveguide is modeled as a 1 cm thick, 28 cm by 30 cm rectangular plate with a 9 cm by 6 cm opening. Figure 3-5 shows the layout of the waveguide at a $\varphi=55°$ and $\theta=55°$ perspective, where φ and θ are the polar coordinate angles. The waveguide consists of two sheets that lie in XY-plane with 1 cm distance in Z-axis, connected by 1 cm long wires in Z-direction. The incident field passes through the opening and gets blocked everywhere else on top of the bowtie. To keep the number of segments low, 1.5-2 cm long wires are used to model the waveguide and broken into 2 segments. The size of the

small rectangular openings of the waveguide is an order smaller than the wavelength and does not pass through any electromagnetic wave.

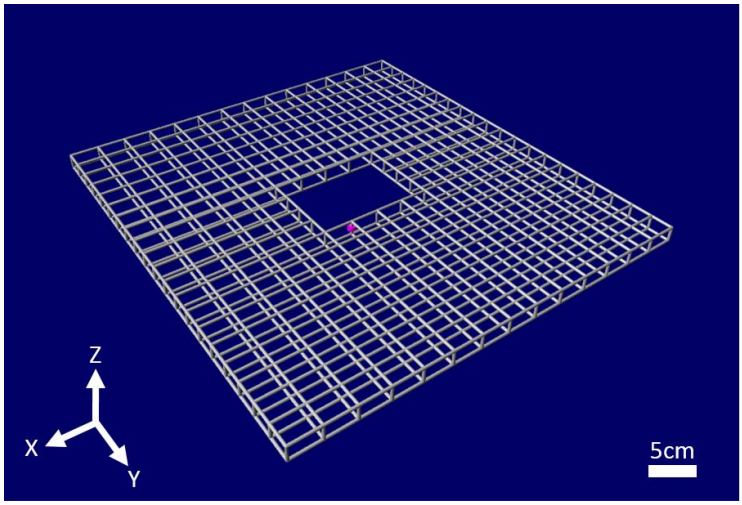

Figure 3-5 NEC 3D View of the waveguide from φ=55° and θ=55° polar coordinate angles. The 9 cm by 6 cm opening passes through the incident field towards the bowtie structure.

Bowtie structures are created by modeling the individual plates, shifting them along X-axis, and duplicating with respect to the YZ-plane by Coordinate Transformation (GM) card. Figure 3-6 shows the layout of the 3/8" thick, 45° bowtie from φ=270° and θ=60° perspective.

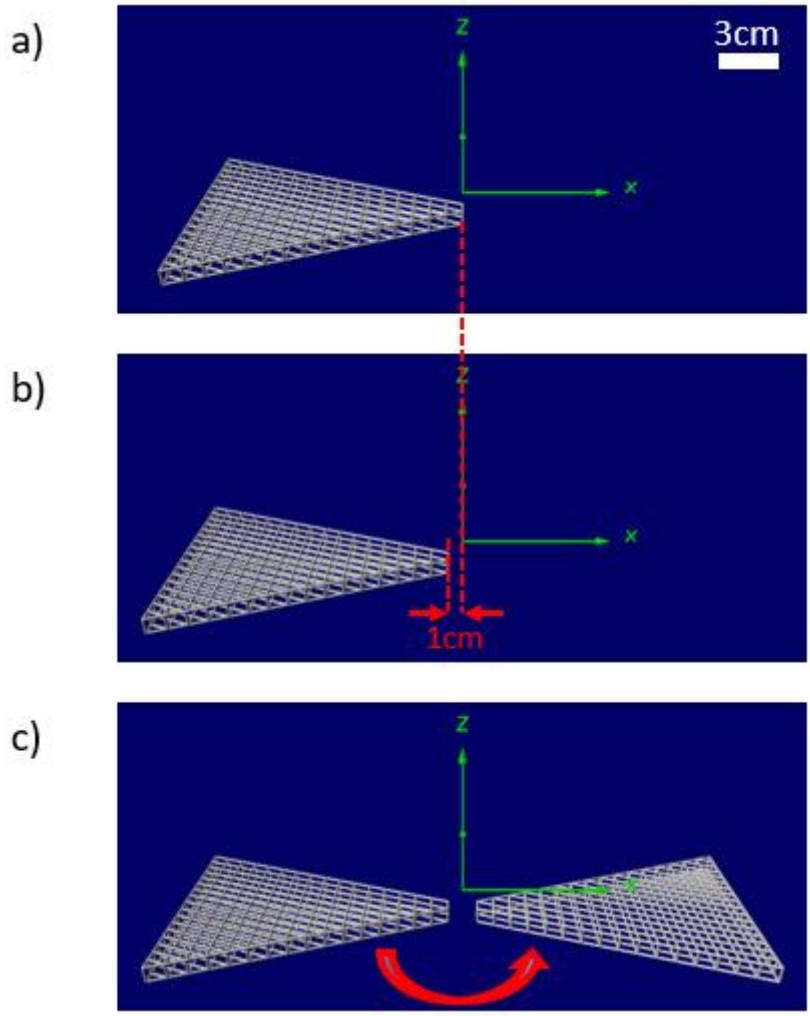

Figure 3-6 NEC 3D View from φ=270° and θ=60° polar coordinate angles. a) 3/8" thick single plate with 45° tip angle is modeled along X-axis with its tip at X=0 and Y=0 coordinates. b) The single plate is shifted in negative X-direction with half the size of desired bowtie gap size (1 cm). c) The bowtie structure that consists of the shifted original plate and its duplicate in YZ-plane, with 2 cm gap size.

The exterior frame of the individual plate is drawn on engineering paper with the exact size of the plate used in the experiment. The frame is then filled out with wires that would evenly distribute the current under incident field excitation. The unfilled rectangular, triangular, or rhombus shapes inside the plate are an order smaller than the wavelength so that the incident field does not penetrate and the plate behaves like solid

metal. The *wire ends*, points that situate a wire in Cartesian coordinates, are obtained from the manual drawing and entered into Microsoft Excel to create the master table that defines the geometry of the wires. NEC input file is then generated with the wire, load, frequency, and other details of the simulation. Similar to the waveguide, the bowtie consists of two sheets in XY-plane connected in Z-direction. The thickness of the bowtie is defined by the distance between the sheets.

The 45° and 90° plates are modeled (Figure 3-7a-b) with 1-1.2 cm long wires, so that each wire consists of one segment. The 135° and 180° plates are not modeled with wires as short as the 45° and 90° plates because the areas are significantly larger and the number of segments exceeds the 8000-segment limitation. Therefore, similar to the waveguide, the large plates are modeled by longer wires. The 135° plate (Figure 3-7c) consists of a triangular tip with 0.6-1 cm long wires that consists of 1 segment each and a rectangular base with 1.5-2 cm long wires that consist of 2 segments each. The 180° plate (Figure 3-7d) consists of 1.5-2 cm long wires that consist of 2 segments each.

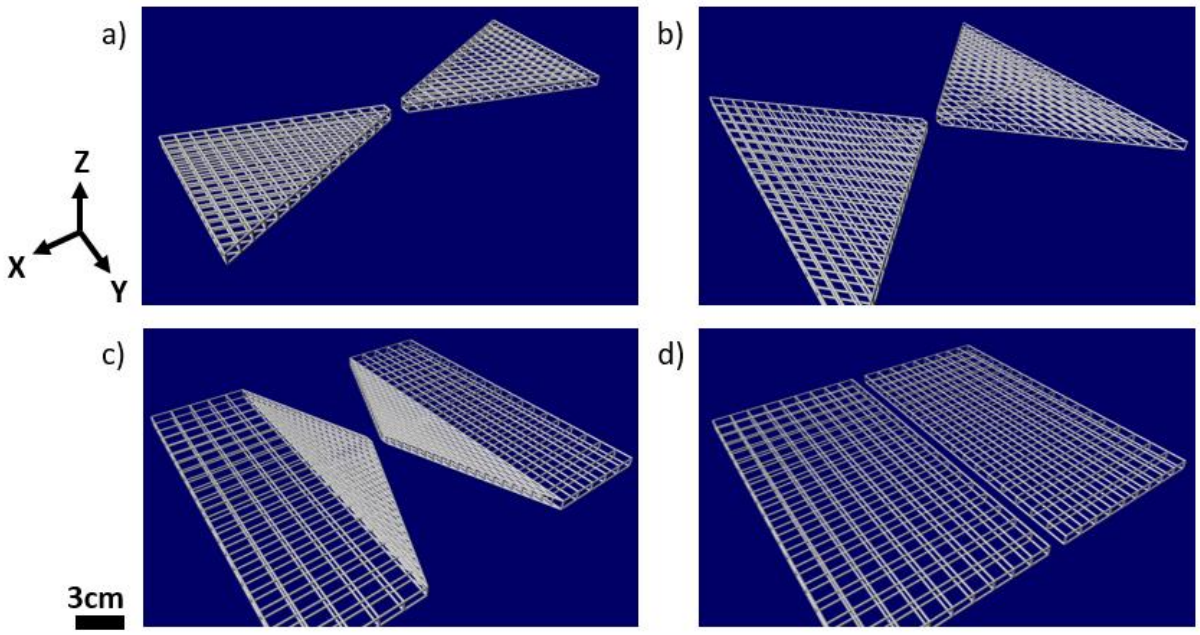

Figure 3-7 Layout of the bowtie structures with 2 cm gap size and different tip angles. a) 45°, b) 90°, c) 135°, and d) 180° tip angles.

The bowtie structure is located underneath the waveguide, exposed to the incident wave coming from the transmitter antenna 2 m above. The distance between the top of the bowtie structure and bottom of the waveguide is fixed at 1.2 cm for all simulations. When the thickness of the bowtie varies, the bottom layer of the bowtie moves in Z-axis while the top layer stays at fixed 1.2 cm from the waveguide. This distance is measured from the center of the wires.

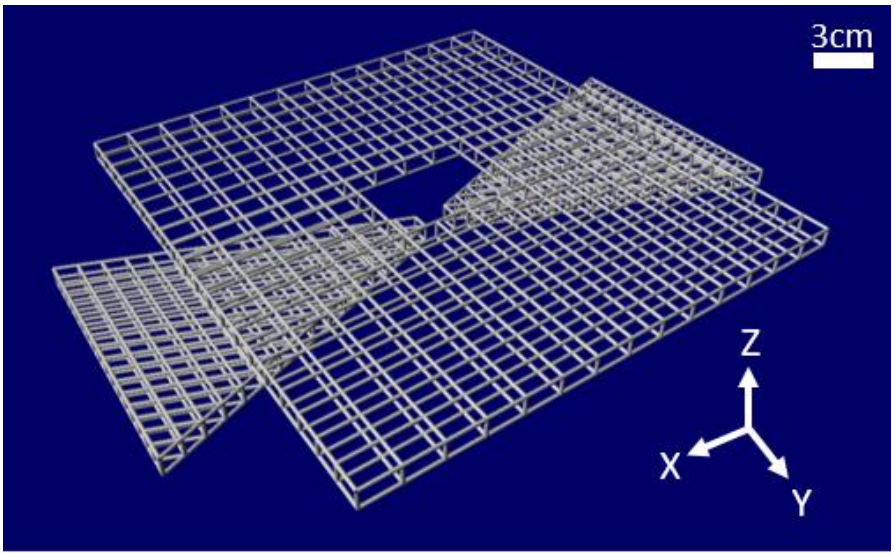

Figure 3-8 Layout of the 45° bowtie structure with 2 cm gap size expose by incident field through the 9 cm by 6 cm opening of the waveguide.

4. Electric Field Simulations and Results

4.1 Electric Field Simulation

To study the electric field enhancement factor due to the bowtie structure, the electric field in the vicinity of the bowtie gap is analyzed. The experimental portion of our work [56] uses a 3 cm long (λ/4) monopole receiver antenna to measure the power of electromagnetic wave of a λ by λ area, centered at the origin of the XY-plane (X=Y=0). Because the antenna and its motorized fixture do not fit inside the small gap of the bowtie, the electromagnetic wave 5 mm below the bowtie structure is measured. The electric field of the same region is calculated by NEC to compare the enhancement factor with the experiment.

The electric fields with and without the bowtie structure are calculated to study the effect of the bowtie. The electric field simulation is performed by the Near Fields (NE) card, which calculates the near electric fields in the region of interest. Figure 4-1 shows the region of interest (in red) underneath the 3/8" thick, 90° bowtie with 10 mm gap size. The electric field of the λ by λ area 5 mm below the bowtie is calculated. With a step increment of 0.5 mm, NEC provides the electric field information of 14,641 points in the λ by λ area.

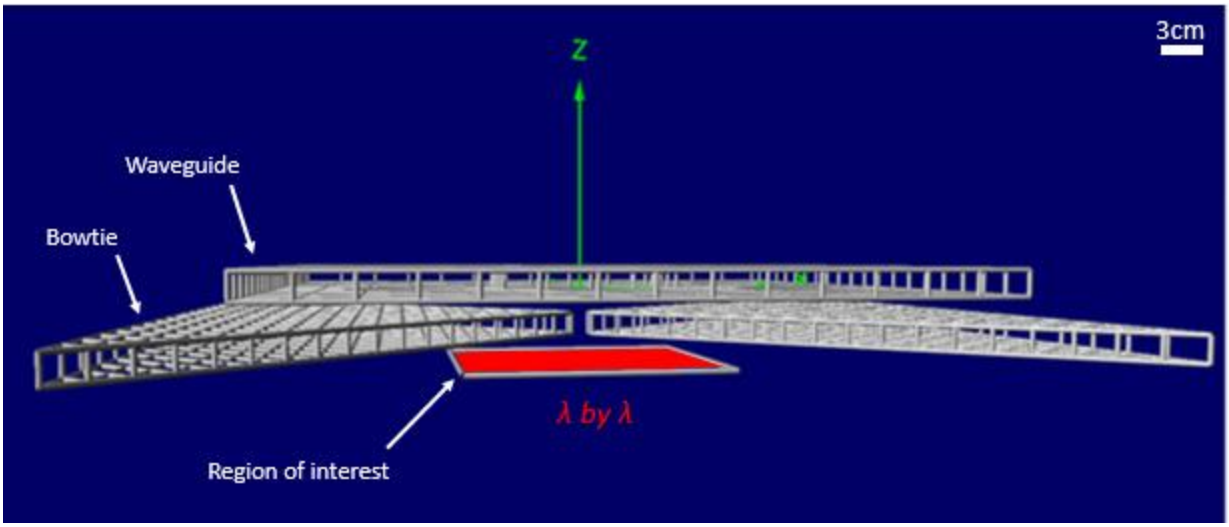

Figure 4-1 Layout of the 3/8" thick, 45° bowtie structure with 10 mm gap size. The electric field at the red dashed line along X-axis from -6 cm to 6 cm under the bowtie structure is calculated and analyzed.

NEC provides X, Y, and Z components of the total electric field at each point specified by the user. The transmitter antenna is positioned to radiate the incident electric field in X-axis and magnetic field in Y-axis. The bowtie structure is modeled along X-axis, with the central axis at Y=0, to interact with the incident field. Therefore, the X component of the total electric field calculated by NEC is of interest to compare and analyze.

4.1.1 Electric Field Enhancement

Figure 4-2 shows the simulation results without (a) and with (b) the 3/8" thick, 90° bowtie structure with 10 mm gap size. The simulation result without bowtie shows unfocused radiation of electric field spread throughout the λ by λ region. The bowtie focuses the electric field towards the gap region and enhances the amplitude significantly.

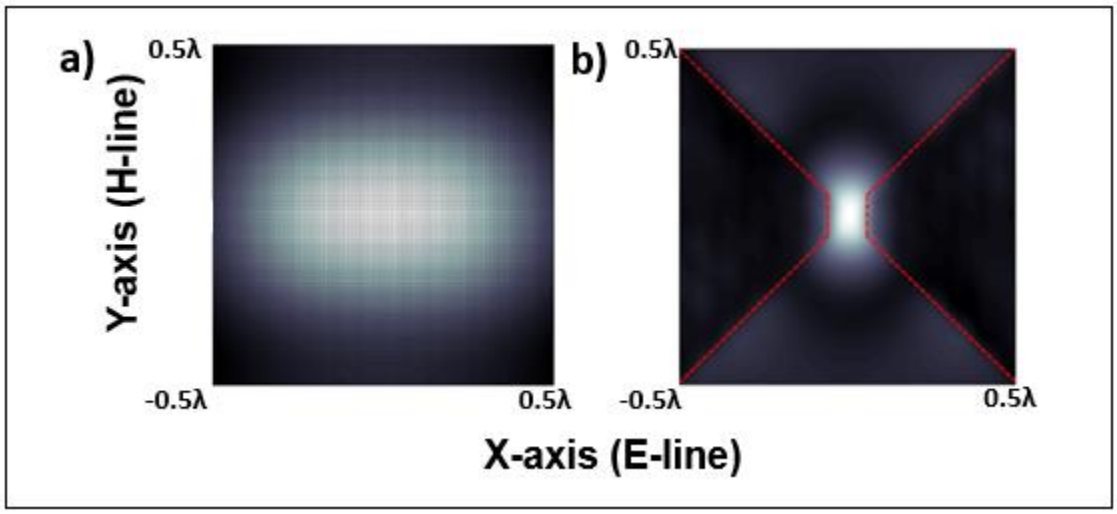

Figure 4-2 The electric field simulation a) without, and b) with 3/8" thick, 90° bowtie with 10 mm gap size. The region of interest is a λ by λ area 5 mm under the bowtie. The bowtie focuses and enhances the electric field at the gap region.

To quantitatively analyze the enhancement and focusing, the electric field along the central axis of the bowtie is selectively studied instead of the entire λ by λ area. The X-axis ranges from -0.5λ to 0.5λ while Y-axis is fixed at 0. Figure 4-3 shows the enhancement and focusing of the electric field due to the bowtie. The Gaussian pattern of the electric field without bowtie structure shows the radiation of the 3 cm long antenna in far field (2 m) from the platform. In presence of the bowtie, the electric field near the gap focuses significantly and increases from 66.8 mV to 286.7 mV/m.

To determine the enhancement factor, the highest electric field amplitude of the no-bowtie simulation results is used to normalize the electric field pattern with bowtie. The ratio of the electric fields is then squared to determine $|E_t|^2$. As explained in Chapter 2, the square of the ratio between electric fields ($|E_t|^2=|E_{gap}|^2/|E_0|^2$) is the electric field enhancement factor. The enhancement factor of the 3/8" thick, 90° bowtie with 10 mm

gap size reaches 18.4, as shown in Figure 4-3b.

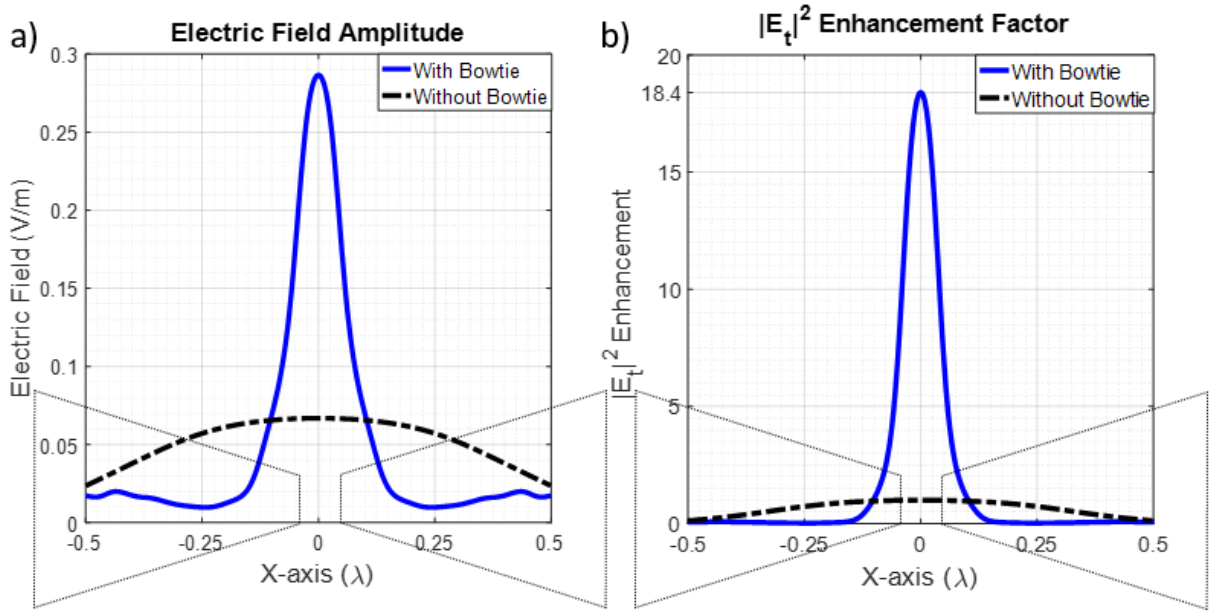

Figure 4-3 a) The electric field simulation results with (solid line) and without (dashed line) 3/8" thick, 90° bowtie structure with 10 mm gap size. b) $|E_t|^2$ enhancement factor. X-axis goes from -6 cm (-0.5λ) to 6 cm (0.5λ). Bowtie gap is drawn to scale, but the rest of the structure is not.

4.2 Geometry Effect on Enhancement Factor

The main objective of the thesis is to find the geometric parameters of the bowtie structure with the highest enhancement factor. The tip angle, thickness, and gap size of the bowtie are modified as shown in Table 3-1 in Chapter 3. With 4 tip angles, 3 thicknesses, and 11 gap sizes, a total of 132 simulations have been performed. Figure 4-4 shows the enhancement factor and gap size relationship of the 3/8" thick 45°, 90°, 135°, and 180° bowtie structures. Even though the enhancement factors are different, the gap size effect on the enhancement pattern of simulation (a) and experiment (b) are in agreement. The 90° bowtie shows the highest enhancement of 19.25 at 8 mm gap size.

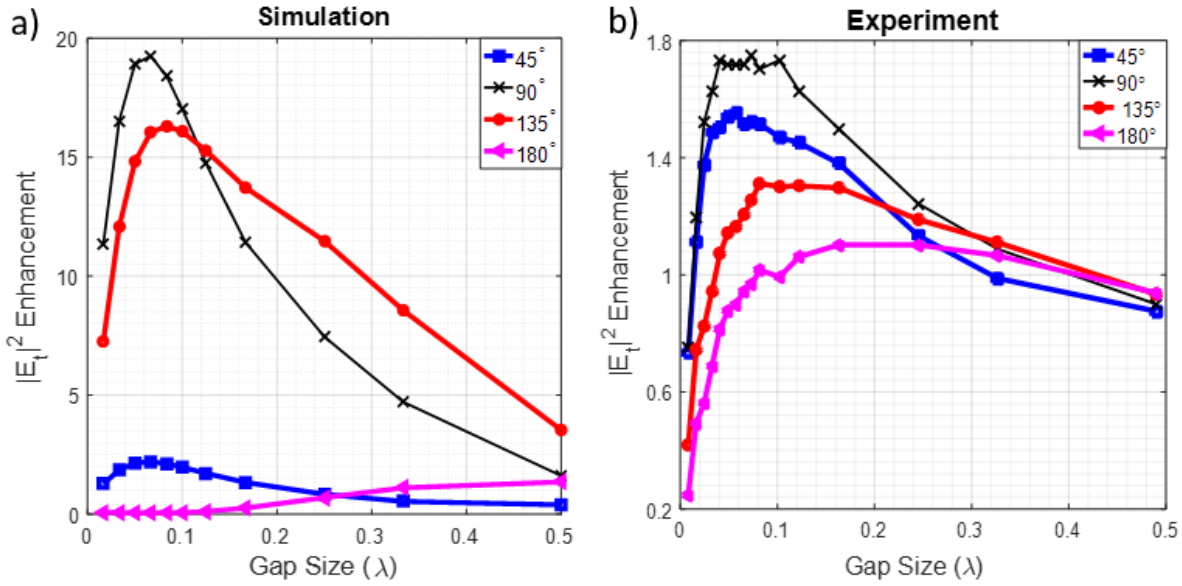

Figure 4-4 a) NEC simulation, and b) experiment $|Et|^2$ enhancement results of 3/8" thick 45°, 90°, 135°, and 180° bowties over varying gap size.

Table 4-1 Comparison of the maximum enhancement factors and the respective gap sizes found by simulation and experiment.

	Simulation		Experiment	
Tip Angle	Maximum Enhancement Factor	Gap Size (mm)	Maximum Enhancement Factor	Gap Size (mm)
45°	2.2	8	1.55	7
90°	**19.25**	**8**	**1.75**	**8**
135°	16.31	10	1.31	10
180°	1.35	60	1.1	30

4.2.1 Tip Angle

The bowtie structure behaves like a receiver antenna under incident field, absorbing the electromagnetic wave energy. The bigger the antenna aperture, the greater the absorbed energy. Figure 3-7 in Chapter 3 shows the NEC 3D view of the bowtie structures. The surface areas of the 45°, 90°, 135°, and 180° bowtie structures are 304.4, 360, 529, and 648 cm^2, respectively. Depending on the gap size, a significant amount of the total effective area is blocked by the waveguide. However, the exposed areas of the 45°, 90°, 135°, and 180° bowties are still in ascending order. The 9 cm by 6 cm opening of the waveguide limits the maximum effective area to 54 cm^2. Therefore, with respect to antenna aperture, the larger tip angle benefits the electric field enhancement.

Another key factor that depends on the tip angle is charge focusing. The electron and hole accumulations flip-flop at the tips of the plates at the incident field frequency. The sharp tip angle focuses the charges into small region while wide tip angle spreads out the accumulation region. At 180°, the bowtie does not have any geometric focusing. Therefore, with respect to charge focusing, the smaller tip angle benefits the electric field enhancement.

The simulation results show that the 90° bowtie structure has the highest electric field enhancement. It is likely due to the tradeoff between the aperture and focusing. Even though the larger tip angle bowtie absorbs more energy, the resultant charges are not focused into the gap region to enhance the incident field, and vice versa. The 90° bowtie structure has high absorption of incident electric field that is physically focused by the tips.

Furthermore, the bowtie structure becomes a self-complementary antenna at 90°, where the shape of the conductor part is identical to the non-conducting part. Figure 4-5 shows some other self-complementary antenna examples.

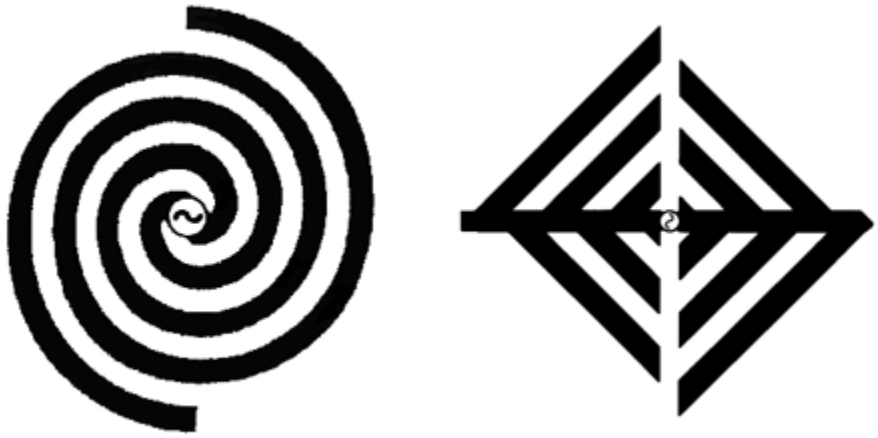

Figure 4-5 Examples of Self-Complementary Antennas [Public Domain Figure].

The self-complementary antennas have constant 188.4 Ω impedance across all frequencies [61]. According to Babinet's principle [62], the impedance of the antenna and its complementary slot can be written as

$$Z_{metal} \cdot Z_{slot} = \frac{\mu}{4\epsilon} \tag{30}$$

where Z_{metal} is the impedance of the antenna, Z_{slot} is the impedance of the complementary slot, μ is the magnetic permeability, and ϵ is the electric permittivity of air. At the incident field frequency of 2.45 GHz, the non-self-complementary bowtie structures could have larger impedance and higher incident field reflection. The self-complementary

antenna with constant impedance provides an optimum balance of aperture size and charge focusing.

4.2.2 Gap Size

The highest electric field enhancement occurs when the gap size of the bowtie structures (45°, 90°, and 135°) is 8-10 mm. In terms of the wavelength, the highest enhancement gap size is 0.067-0.083 λ. As shown in Table 4-2, no specific relationship between the incident wavelength and gap size of the 90° bowtie is observed when the incident field frequency changes.

Table 4-2 The maximum enhancement gap sizes of the 90° bowtie at different incident field frequencies.

Incident frequency (GHz)	Incident wavelength (mm)	Maximum enhancement gap size (mm)	Gap size in terms of wavelength (λ)
2.4	125	6	0.048
2.5	120	4	0.033
3	100	9	0.09

To study the effect of tip width (shown in Figure 3-4 of Chapter 3) on enhancement, the 1 cm wide truncated tips of the 90° bowtie are modified to non-truncated, sharp tips. The simulations are performed by varying the gap size while the other variables (tip angle 90°, thickness 3/8") are fixed.

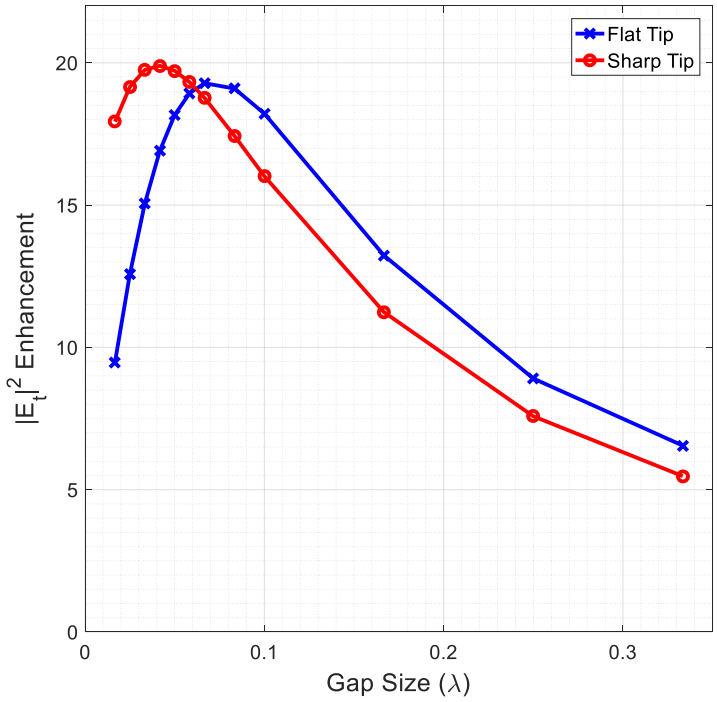

Figure 4-6 The effect of tip width change (from flat to sharp) on maximum electric field enhancement and optimal gap size.

As shown in Figure 4-6, the highest electric field enhancement occurs at smaller gap size, 5 mm, in sharp tip bowtie compared to flat tip bowtie. However, the enhancement factor is not affected significantly, as there is only 3% increase.

4.2.3 Thickness

The thickness of the metal plates could affect the incident field absorption and thus the enhancement factor. In nanoparticle studies discussed in Chapter 2, the thickness is typically much smaller than the width and length of the particle. To preserve this ratio in macroscale, the thickness of the bowties are varied as 1/8”, 1/4”, and 3/8”. However,

the thickness does not affect the maximum enhancement factor and the gap size where it is maximum. Table 4-3 shows the results of the 90° bowtie structures.

Table 4-3 The maximum enhancement factor and gap size of the 1/8", 1/4", and 3/8" thick 90° bowtie structures.

Thickness (inch)	1/8	1/4	3/8
$\|E_t\|^2$	18.45	17.64	19.25
Gap size (mm)	9	9	8

The skin depth is an outer region of a conductor where majority (63%) of the current flows. At 2.45 GHz, the skin depth of aluminum is calculated as [63]

$$\delta_S = \sqrt{\frac{1}{\pi f \mu \sigma}} = 1.655\ \mu m = 65.17\ \mu inch \qquad (31)$$

where σ is the conductivity of aluminum (36.9×10^6 S/m). This skin depth of aluminum suggests that the electrons flow on the outer 0.01-0.05% of the 1/8", 1/4", and 3/8" bowties. Therefore, the thickness of the bowtie does not affect the enhancement factor significantly, which agrees with the results shown in Table 4-3. However, the thickness may affect the enhancement factor when it is comparable to the skin depth.

4.3 Mode Volume

As discussed in Chapter 2, the surface-enhanced Raman spectroscopy achieved the electric field enhancement of 10^{14}-10^{15}. Other studies of nanoparticles with different

sizes and shapes demonstrated $|E_t|^2$ enhancement factor up to 10^6. However, in macroscale simulation, the enhancement factor is significantly low. Myung-Ki Kim *et al*. has demonstrated the volume dependency of plasmonic focusing and argued that the relationship between the mode volume and enhancement factor is a representation of the plasmon focusing: the more focused the plasmons are in a small volume, the higher the enhancement factor is [17]. The mode volume is a region where the plasmons are focused and electric field enhancement is strong. Mode volume is a dimensionless unit in terms of the cubit wavelength (λ^3).

To analyze and compare this result in macroscale, the mode volume of the enhancement region is studied. In this thesis, the mode volume is defined by the region where electric field is greater than 1/e (36%) of its maximum. The electric field of a 2 x 3 x 3 cm^3 region surrounding the 3/8" thick 90° bowtie with 8 mm gap size is simulated. The resolution of the region is 0.1 mm, resulting in a total 1,030,301 data points. A total of 547,548 data points are eliminated as their electric fields are smaller than 1/e (36%). The remaining 482,753 data points amount to a mode volume of 8.4 cm^3 out of the simulated 18 cm^3. Figure 4-7 shows the electric field pattern of the mode volume in XY, XZ, and YZ planes.

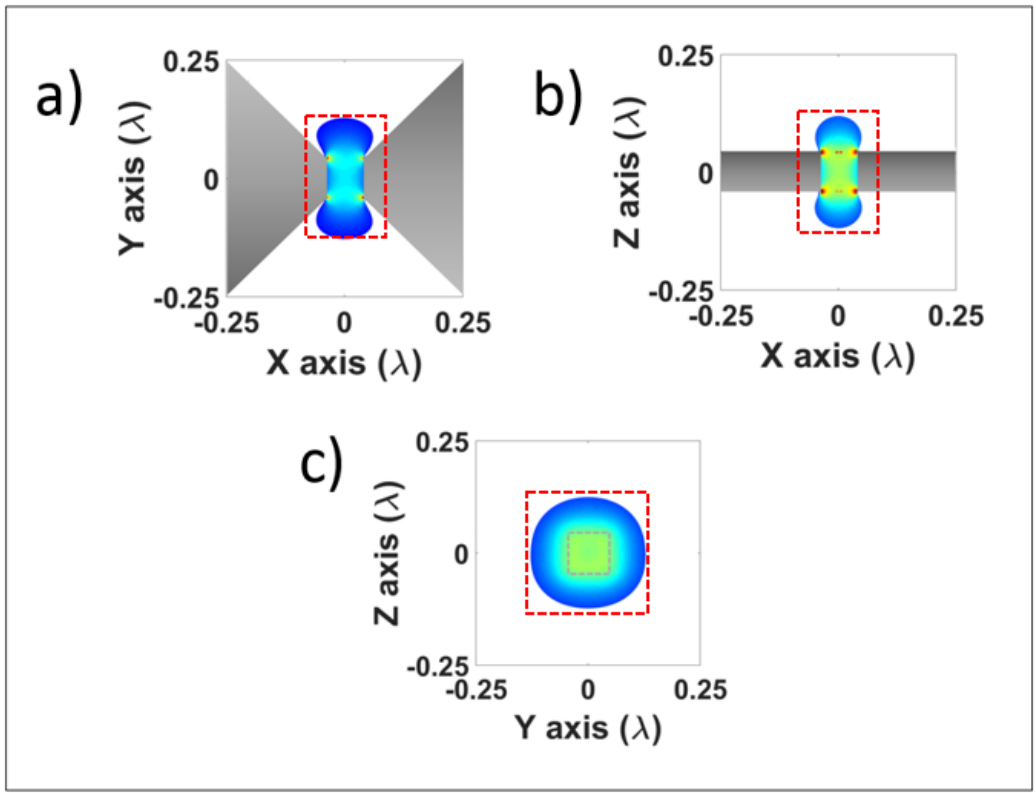

Figure 4-7 The mode volume simulation based on electric field patterns in a) XY, b) XZ, and c) YZ planes. The electric field greater than 1/e (36%) of the maximum is shown. Red dashed box is the 2 x 3 x 3 cm^3 simulation region.

The mode volume simulation shows that the electric field is enhanced in a wide region surrounding the bowtie gap. The mode volume is 8.8 times larger than the 1 x 1 x 0.95 cm^3 region directly in between the faces of the truncated triangular plates. As explained in Chapter 2, the mode volume is calculated in terms of λ as

$$V_{mode} = \frac{8.4\ cm^3}{(12.24\ cm)^3} = 4.57 \cdot 10^{-3}\ \lambda^3$$

The combination of the enhancement factor and mode volume, the volumetric enhancement factor, is found in macroscale and nanoscale, and compared in Table 4-4. Myung-Ki Kim *et al*. varied the mode volume by modifying the structure and found the

enhancement factor varies accordingly, while the volumetric enhancement factor is consistently on the order of 10^{-2}.

$$V.E = V_{mode} \cdot |E_t|^2 \tag{32}$$

Table 4-4 The volumetric enhancement factors in macroscale and nanoscale.

	$\|E_t\|^2$	V_{mode} (λ^3)	Volumetric Enhancement Factor
Macroscale	19.25	0.00457	0.088
Nanoscale	400000	$1.3 \cdot 10^{-7}$	0.052

5. Conclusion and Future Work

5.1 Conclusion

In this thesis, the optimal geometry of the bowtie gap for maximum electric field enhancement is studied by NEC antenna modeling system. The simulations are performed by creating the experimental platform using aluminum antenna segments. Under the incident field excitation, the metallic bowtie structure focuses and enhances the electric field into the gap region. The enhanced electric field is used for applications such as subwavelength imaging and single molecule detection.

Subwavelength size objects such as molecules and viruses require imaging techniques more advanced than the conventional optical microscope. Using the plasmonic properties of metal nanoparticles, surface-enhanced Raman spectroscopy has demonstrated electric field enhancement factor of 10^{14}-10^{15} and single molecule detection. However, depending on the size and shape of the nanoparticles, the enhancement factor results have been inconsistent and unpredictable. Further studies are required to optimize the geometric parameters of the metal nanoparticles for maximum electric field enhancement. Fabricating the nanoparticles with precise incremental geometry variations, however, is challenging.

This thesis studies the geometry effects of the metal bowtie structure on electric field enhancement in macroscale at radio frequency of 2.45 GHz. Even though the plasmonic resonance of the free electrons does not occur in macroscale, the effects of shape and gap size on the electron focusing and coupling can be studied. To find the optimal geometry of the bowtie, the electric field enhancement is studied while the tip

angle, thickness, and gap size are varied. The results are applicable in nanoscale bowtie structures to generate maximum electric field enhancement.

The bowtie structures demonstrated different electric field enhancement results depending on their abilities to absorb and focus the incident field. In macroscale, the thickness of the bowtie has little to no effect on the enhancement factor because it is significantly larger than the skin depth in radio frequency. Large angle bowties (135° and 180°) have high antenna aperture of incident field but weak focusing of the electrons. Small angle bowties (45°) can focus the electrons to the gap region more efficiently but have low antenna aperture.

The 90° bowties are self-complementary antennas with high electric field enhancement due to the combination of high absorption and electron focusing. The 90° bowtie with 8 mm (0.065 λ) gap size has the maximum electric field enhancement factor of 19.25. To supplement the SERS by providing the maximum electric field enhancement, the bowtie-shaped nanostructures with 90° tip angle should be fabricated on the substrate.

5.2 Future Work

There are a few points that need to be addressed for future work on the optimization of geometry for a maximum electric field enhancement.

First, the thickness of the bowtie structure does not affect the enhancement factor in macroscale because it is significantly larger than the skin depth. This assertion should be verified in nanoscale where the skin depth is comparable to the thickness of the nanoparticles. Furthermore, the effect of thickness on the electric field enhancement

should be studied because it is one of the important variables that can be easily modified to obtain the maximum enhancement factor.

Second, this study shows no relationship between the maximum enhancement gap size and other geometric parameters. The maximum enhancement gap size has been consistently 8-10 mm for different tip angles. Furthermore, no mathematical relationship was found between the maximum enhancement gap size and incident wavelength. The maximum enhancement gap size does not change proportionally when the incident radio frequency changes from 2.0 GHz to 3.0 GHz. The bowtie with sharp, non-truncated tips reduced the maximum enhancement gap size by 3 mm, which still does not suggest any geometric relationship. Therefore, the optimal gap size in nanoscale bowtie structure cannot be deduced based on the results of this thesis. To optimize the gap size in nanoscale, further studies are required by varying other parameters such as the height, width, and thickness (comparable to the skin depth) of the bowtie.

Lastly, other simulation platforms such as MATLAB's *Antenna Modeling and Analysis*, ARRL's *Antenna Modeling*, or Massachusetts Institute of Technology's *MEEP* could be used to study the electric field enhancement factors of similar structures. The NEC simulation results presented in this thesis are significantly larger than the experiment results of the same setup, which is explained by a higher coupling efficiency and lower Joule losses. Further studies using different platforms could confirm the difference between simulation and experiment, which could help predict the enhancement factor in nanoscale experiments.

BIBLIOGRAPHY

[1] Lloyd, Geoffrey Ernest Richard. *Aristotle: the growth and structure of his thought*. Cambridge University Press, 1968.

[2] Lawson, Russell M. *Science in the ancient world: an encyclopedia*. ABC-CLIO, 2004.

[3] Galilei, Galileo. *Discoveries and opinions of Galileo: including The starry messenger (1610), Letter to the Grand Duchess Christina (1615), and excerpts from Letters on sunspots (1613), The assayer (1623)*. Vol. 94. Anchor Books, 1957.

[4] Croft, William J. *Under the microscope: a brief history of microscopy*. Vol. 5. World Scientific, 2006.

[5] Shalek, Alex K., et al. "Single-cell transcriptomics reveals bimodality in expression and splicing in immune cells." *Nature* 498.7453 (2013): 236-240.

[6] Dominguez, Maria H., et al. "Highly multiplexed quantitation of gene expression on single cells." *Journal of immunological methods* 391.1 (2013): 133-145.

[7] Davidson, Michael W. "Microscope objectives: Numerical aperture and resolution." www.micro.magnet.fsu.edu/primer/anatomy/numaperture.html. Accessed 01 Jun. 2016.

[8] Saha, Swapan K. *Diffraction limited imaging with large and moderate telescopes*. World Scientific, 2007.

[9] Siebert, Friedrich, and Peter Hildebrandt. *Vibrational spectroscopy in life science*. John Wiley & Sons, 2008.

[10] Betzig, Eric, and Jay K. Trautman. "Near-field optics: microscopy, spectroscopy, and surface modification beyond the diffraction limit." *Science*257.5067 (1992): 189-195.

[11] Reynolds, Edward S. "The use of lead citrate at high pH as an electron-opaque stain in electron microscopy." *The Journal of cell biology* 17.1 (1963): 208-212.

[12] Selvin, Paul R., and Taekjip Ha. *Single-molecule techniques*. Cold Spring Harbor Laboratory Press, 2008.

[13] Neuman, Keir C., and Attila Nagy. "Single-molecule force spectroscopy: optical tweezers, magnetic tweezers and atomic force microscopy." *Nature methods* 5.6 (2008): 491.

[14] Staveley, Lionel Alfred Kilby. *The characterization of chemical purity: organic compounds*. Elsevier, 2016.

[15] Colthup, Norman. *Introduction to infrared and Raman spectroscopy*. Elsevier, 2012.

[16] Geim, Andre K., and Konstantin S. Novoselov. "The rise of graphene." *Nature materials* 6.3 (2007): 183-191.

[17] Kim, Myung-Ki, et al. "Squeezing Photons into a Point-Like Space." *Nano letters* 15.6 (2015): 4102-4107.

[18] Shimanouchi, Takehiko. "Tables of molecular vibrational frequencies. Consolidated volume II." *Journal of physical and chemical reference data* 6.3 (1977): 993-1102.

[19] Jeanmaire, David L., and Richard P. Van Duyne. "Surface Raman spectroelectrochemistry: Part I. Heterocyclic, aromatic, and aliphatic amines adsorbed on the anodized silver electrode." *Journal of Electroanalytical Chemistry and Interfacial Electrochemistry* 84.1 (1977): 1-20.

[20] Smalyukh, Ivan I. "Plasmonic nanoparticles & nanostructures." University of Colorado, Boulder. July 27-August 7, 2015.

[21] Davaji, B., et al. "In-vivo single cell protein interaction investigation using microfluidic platform." 2015 Transducers-2015 18th International Conference on Solid-State Sensors, Actuators and Microsystems (TRANSDUCERS). IEEE, 2015.

[22] Spring, K. R., and M. W. Davidson. "Introduction to fluorescence microscopy. Nikon Microscopy U." (2008).

[23] Zernike, Frits. "How I discovered phase contrast." *Science* 121.3141 (1955): 345-349.

[24] Phillips, Stephen J. "Phase contrast and interference microscopy for cell biologists KFA Ross. New York: St. Martin's Press, 1967. 238 pp."*Cancer Research* 28.10 (1968): 2170-2170.

[25] Sheldrick, B. "Structure determination by X-ray crystallography: by MFC Ladd and RA Palmer. pp 502. Plenum Press, New York. ISBN 0-30641878-9." (1986): 93.

[26] Solomon, B., L. Berg, and D. Martin. "Biology, 6th." *Belmont, CA: Thomson Brooks/Cole* (2002).

[27] Drinking water contaminants -organic chemicals - Benzene. Water.epa.gov. Accessed 01 Jun. 2016.

[28] Walt, David R. "Optical methods for single molecule detection and analysis." *Analytical chemistry* 85.3 (2012): 1258-1263.

[29] Yeh, Hsin-Chih, et al. "Single-molecule detection and probe strategies for rapid and ultrasensitive genomic detection." *Current pharmaceutical biotechnology* 6.6 (2005): 453-461.

[30] Heavens, Oliver S., and Robert W. Ditchburn. *Insight into optics*. Chichester, West Sussex,, England: Wiley, 1991.

[31] Tremblay, Christian. "Waves." www.mrtremblaycambridge.weebly.com/15-waves.html. Accessed 01 Jun. 2016.

[32] Airy, G. B., "On the diffraction of an object-glass with circular aperture," *Transactions of the Cambridge Philosophical Society*, Vol. 5, 1835, p. 287.

[33] Lipson, Ariel, Stephen G. Lipson, and Henry Lipson. *Optical physics*. Cambridge University Press, 2010.

[34] Ferrari, A. C., et al. "Raman spectrum of graphene and graphene layers." *Physical review letters* 97.18 (2006): 187401.

[35] McCreery, Richard L. *Raman spectroscopy for chemical analysis*. Vol. 225. John Wiley & Sons, 2005.

[36] Semrock. "Filter types for Raman spectroscopy applications." www.semrock.com/filter-types-for-raman-spectroscopy-applications.aspx. Accessed 01 Jun. 2016.

[37] Levy, Y., et al. "Raman scattering of thin films as a waveguide." *Optics communications* 11.1 (1974): 66-69.

[38] Albrecht, M. Grant, and J. Alan Creighton. "Anomalously intense Raman spectra of pyridine at a silver electrode." *Journal of the American Chemical Society* 99.15 (1977): 5215-5217.

[39] Tsang, J. C., J. R. Kirtley, and J. A. Bradley. "Surface-enhanced Raman spectroscopy and surface plasmons." *Physical Review Letters* 43.11 (1979): 772.

[40] Rowe, J. E., et al. "Ultrahigh-vacuum studies of enhanced Raman scattering from pyridine on Ag surfaces." *Physical Review Letters* 44.26 (1980): 1770.

[41] Maier, Stefan Alexander. *Plasmonics: fundamentals and applications*. Springer Science & Business Media, 2007.

[42] Jain, Prashant K., and Mostafa A. El-Sayed. "Plasmonic coupling in noble metal nanostructures." *Chemical Physics Letters* 487.4 (2010): 153-164.

[43] Murata, Ken-ichiro, and Hajime Tanaka. "Surface-wetting effects on the liquid–liquid transition of a single-component molecular liquid." *Nature communications* 1 (2010): 16.

[44] Le Ru, E. C., and P. G. Etchegoin. "Rigorous justification of the| E| 4 enhancement factor in surface enhanced Raman spectroscopy." *chemical Physics letters* 423.1 (2006): 63-66.

[45] Talley, Chad E., et al. "Surface-enhanced Raman scattering from individual Au nanoparticles and nanoparticle dimer substrates." *Nano letters* 5.8 (2005): 1569-1574.

[46] Hardy, Mike, et al. "Detection of low-concentration contaminants in solution by exploiting chemical derivatization in surface-enhanced Raman spectroscopy." *Analytical chemistry* 86.18 (2014): 9006-9012.

[47] Nie, Shuming, and Steven R. Emory. "Probing single molecules and single nanoparticles by surface-enhanced Raman scattering." *science* 275.5303 (1997): 1102-1106.

[48] Michaels, Amy M., M. Nirmal, and L. E. Brus. "Surface enhanced Raman spectroscopy of individual rhodamine 6G molecules on large Ag nanocrystals." *Journal of the American Chemical Society* 121.43 (1999): 9932-9939.

[49] Orendorff, Christopher J., et al. "Surface-enhanced Raman spectroscopy of self-assembled monolayers: sandwich architecture and nanoparticle shape dependence." *Analytical chemistry* 77.10 (2005): 3261-3266.

[50] Kurukshetra, Haryana. "Recent Developments, Issues and Challenges for Lithography in ULSI Fabrication."

[51] Denomme, Ryan C., et al. "Nanoparticle fabrication by geometrically confined nanosphere lithography." *Journal of Micro/Nanolithography, MEMS, and MOEMS* 12.3 (2013): 031106-031106.

[52] Haynes, Christy L., et al. "Angle-resolved nanosphere lithography: manipulation of nanoparticle size, shape, and interparticle spacing." *The Journal of Physical Chemistry B* 106.8 (2002): 1898-1902.

[53] Hulteen, John C., and Richard P. Van Duyne. "Nanosphere lithography: a materials general fabrication process for periodic particle array surfaces."*Journal of Vacuum Science & Technology A* 13.3 (1995): 1553-1558.

[54] Ansar, Siyam M., et al. "Quantitative comparison of Raman activities, SERS activities, and SERS enhancement factors of organothiols: Implication to chemical enhancement." *The journal of physical chemistry letters* 3.5 (2012): 560-565.

[55] Grober, Robert D., Robert J. Schoelkopf, and Daniel E. Prober. "Optical antenna: Towards a unity efficiency near-field optical probe." *Applied Physics Letters* 70.11 (1997): 1354-1356.

[56] Malakoutian, Mohamadali, et al. "Optimization of the Bowtie Gap Geometry for a Maximum Electric Field Enhancement." *Plasmonics* (2016): 1-6.

[57] Richie, James E., and Tony J. Barrett. "VHF helicopter antennas that incorporate the airframe and reduce rotor modulation." *IEEE transactions on electromagnetic compatibility* 42.3 (2000): 298-302.

[58] Richie, James E., and Benjamin R. Koch. "The use of side-mounted loop antennas on platforms to obtain nearly omnidirectional radiation." *IEEE transactions on antennas and propagation* 53.12 (2005): 3915-3919.

[59] Burke, Gerald J., and A. J. Poggio. "Numerical electromagnetics code (NEC)-method of moments." (1981): 87.

[60] Richie, James E. “The Numerical Electromagnetics Code, NEC. Technical Report # 23.” (1999)

[61] Mushiake, Yasuto. "Origination of Self-Complementary Planar Structures and Discovery of Their Constant-Impedance Property." *Self-Complementary Antennas*. Springer London, 1996. 25-30.

[62] Booker, Henry G. "Slot aerials and their relation to complementary wire aerials (Babinet’s principle)." *J. IEE* 93.pt III (1946): 620-626.

[63] Hayt Jr, William H. "Engineering Electromagnetics 1989." 229-231.

Appendix A: Published Journal Paper

Plasmonics
DOI 10.1007/s11468-016-0262-x

Optimization of the Bowtie Gap Geometry for a Maximum Electric Field Enhancement

Mohamadali Malakoutian[1] · Tsenguun Byambadorj[2] · Benyamin Davaji[1] · James Richie[2] · Chung Hoon Lee[1]

Received: 7 March 2016 / Accepted: 9 May 2016

Abstract Optimization of the geometry of a metallic bowtie gap at radio frequency is presented. We investigate the geometry of the bowtie gap including gap size, tip width, metal thickness and tip angle at macroscale to find the maximum electric field enhancement across the gap. The results indicate that 90° bowtie with 0.06 λ gap size has the most $|E_t|^2$ enhancement. Effects of changing the permittivity and conductivity of the material across the gap are also investigated. NEC-2 simulations show that the numerical calculations agree with the experimental results. Since the design and fabrication of a plasmonic device (nanogap) at nanoscale is challenging, the results of this study can be used to estimate the best design parameters for nanogap structure. Different amounts of enhancement at different frequency ranges are explained by mode volume. The product of the mode volume and $|E_t|^2$ enhancement is constant for different gap structures and different frequencies.

Keywords Electric field enhancement · Plasmonics · Bowtie gap · Mode volume

✉ Chung Hoon Lee
chunghoon.lee@marquette.edu

[1] Nanoscale Devices Laboratory, Marquette University, 1250 W. Wisconsin Avenue, Milwaukee, WI 53233, USA

[2] Microwave Laboratory, Marquette University, 1250 W. Wisconsin Avenue, Milwaukee, WI 53233, USA

Introduction

In recent years, the study of electromagnetic field enhancement has made significant developments in near field imaging, due to the ability of near-field imaging to overcome the diffraction limit [1–5]. A large localized electric field is necessary for near field imaging to characterize materials. It is also required for near-field imaging in fields such as chemistry, biology, medicine, pharmacology, environmental science, and energy saving [6–14]. For instance, a large localized electric field can be used to study a single molecule [15]. Single-molecule analysis has distinct advantages over bulk analysis. Single molecule analysis yields detailed statistical distributions of individual molecule properties instead of the averages of the bulk [16–18].

One way to obtain a large localized electric field is plasmonics. Plasmonics is the interaction between electromagnetic field and free electrons in a metal. Collective oscillations of the free electrons in metal can be induced by an applied electric field. Plasmonics in a nano-structure can result in a localized and enhanced electric field [19–27]. The amount of enhancement depends on various parameters. The size, shape, and thickness of metal films influence the coupling efficiency between the metal and incident field, and result in different enhancement factors [28]. Plasmonics has been studied at nanoscale. However, designing the geometry at nanoscale to study the effects is challenging. Therefore, radio frequency electromagnetic field source and macroscale metal structures are used here to study structural effects to determine the optimal design parameters.

Metals may behave very differently in radio and optical frequencies due to the permittivity of the material, which depends on the damping and plasma frequencies [29, 30].

Published online: 04 June 2016

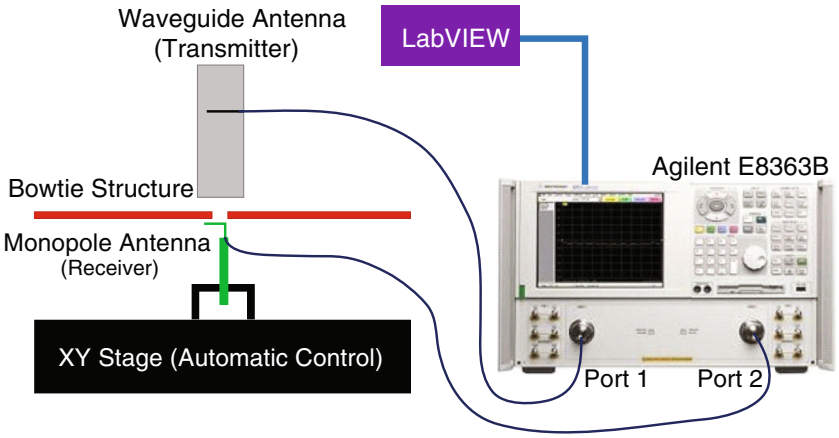

Fig. 1 Experimental setup. This setup includes VNA, transmitter, receiver, bowtie structure, and XY stage

However, metals such as gold, silver, and aluminum are highly reflective at both radio and optical frequencies a few orders of magnitude below the plasma frequency due to their low skin depths. Therefore, this work can be scaled up to optical frequency because aluminum is still highly reflective.

The purpose of this study is to provide the optimum bowtie structure geometry for maximum enhancement efficiency at radio frequency. The bowtie structure consists of two aluminum plates, placed tip-to-tip with adjustable gap. The parameters of the geometry are tip angle, thickness, and gap size. Simulations are performed to confirm the results. In this paper, the second section consists of the description of the bowtie structure. Then, the experimental and simulation setups are explained. Optimization of the experimental setup is also described. In the third section, the results of the experiment and simulation are presented. The results are discussed in detail in the last section.

Method

The experimental setup is shown in Fig. 1. It consists of a waveguide, monopole antenna, bowtie structure, Vector Network Analyzer (VNA), XY-axis motorized stage, and computer. An open-ended rectangular waveguide is used as the transmitter. The waveguide is designed for TE_{10} mode (dominant mode), where 1.6 and 3.1 GHz are the lower and upper cutoff frequencies. The TE (transverse electric) signifies that all electric fields are transverse to the direction of propagation and that no longitudinal electric field is present [31].

A monopole antenna is used as the receiver for transmitted electric field. This antenna has been designed to have minimum return loss between 2.4 and 2.5 GHz. To scan the pattern of transmitted electric field through the bowtie, the monopole antenna is mounted on the motorized XY-axis stage.

In this paper, the electric field enhancement is described in terms of $|E_t|^2$ ($= |E_{gap}|^2/|E_o|^2$), which is the magnitude squared of the electric field across the gap (E_{gap}) divided by electric field without bowtie structure (E_o). The amount of $|E_t|^2$ is investigated for various geometric parameters. The optimal condition for maximum enhancement in our experiment is found from these results.

The geometry of the bowtie gap has significant impact on the electric field enhancement. A previous paper [32] studied the effect of a gap fixed at 90° angle, 1 cm gap size, and 3/8" thickness. In this study, we present the $|E_t|^2$ enhancement at different angles (θ), thicknesses (t), and gap sizes (d). The bowtie structure is placed in XY-plane (E- and H-line), as shown in Fig. 2. The parameter values are given in Table 1.

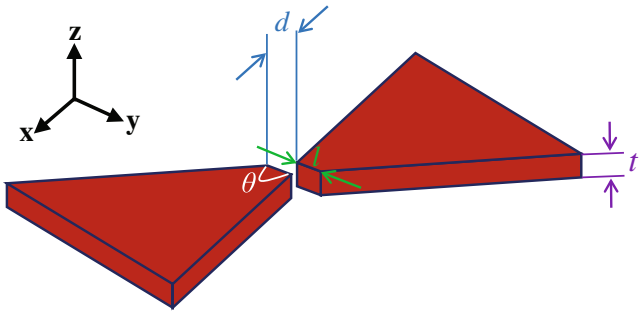

Fig. 2 Layout of the bowtie geometry, where d, l, t, and θ are the gap size, tip width, plate thickness, and gap angle, respectively. E-line and H-line are along x-axis and y-axis in the gap area, respectively

Table 1 Parameters of the bowtie geometry

Parameters	Angle (θ)	Thickness (t)	Gap size (d)
Range	45°	1/8"	$0 - 0.5\lambda$
	90°	1/4"	
	135°	3/8"	
	180°		

The monopole antenna is mounted on the XY stage to scan the area of interest. The stage and VNA are controlled by a custom LabVIEW program and measured data is stored in the computer. The waveguide is connected to port 1 of the VNA as a transmitter and the monopole antenna is connected to port 2 as a receiver. The open end of the waveguide is placed 1.2 cm above the bowtie and the receiver is located 0.5 cm under it. The data is collected at a position five times and the result is averaged.

First, the optimal frequency for the experiment is investigated. Figure 3 shows that 2.45 GHz is most suitable for further experiments as the reflection (S_{11}) is lowest and transmission (S_{21}) is highest. Lowest reflection means the majority of the output power will be applied to the metal plate.

All experimental measurements are simulated on NEC-2 software to compare the results [33]. The model consists of over 5000 segments, each of which has length and radius under one tenth of wavelength and one eighth of segment length, respectively. The waveguide is modeled by placing a 3-cm-long aluminum antenna 2 m ($>$ 15 λ) above the bowtie along X-axis, exciting it with voltage. The unwanted electric field is eliminated with a rectangular structure with same size opening as the experimental waveguide. Therefore, the signal reaching the gap is far-field electric field, being enhanced by the gap. A single-point electric field measurement is performed on the transmitted electric field below the bowtie gap with a resolution of 0.5 mm. Of all the output results, the amplitude of the X-axis electric field is of interest because the experimental receiver antenna is polarized in that direction.

Results

In this section, we present the experimental and simulation results to show the field enhancement as a function of the geometric parameters. The measured data is collected over $\lambda \times \lambda$ area (where λ is the free space wavelength of the incident field). Figure 4 shows the $|E_t|^2$ measurements with and without the bowtie structure between the transmitter and the receiver. In presence of the bowtie (Fig. 4b), there is a bright spot at the center of the image, indicating more focused and enhanced intensity compared to the plain measurement (Fig. 4a). Figure 4c shows the E-cutline through the 3D map, where the $|E_t|^2$ enhancement with gap (dashed line) is about two times bigger than the case without the gap (dotted line). The reported $|E_t|^2$ enhancement in the previous work [32]

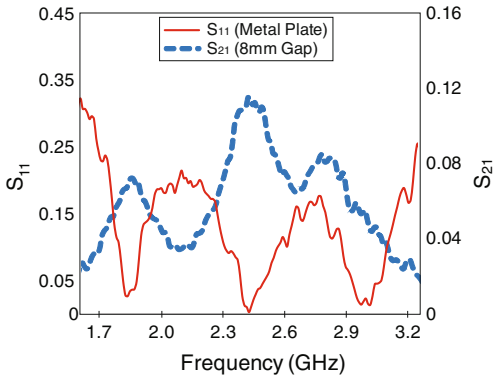

Fig. 3 Measurement of S_{11} with *square* metal plate and S_{21} with bowtie gap

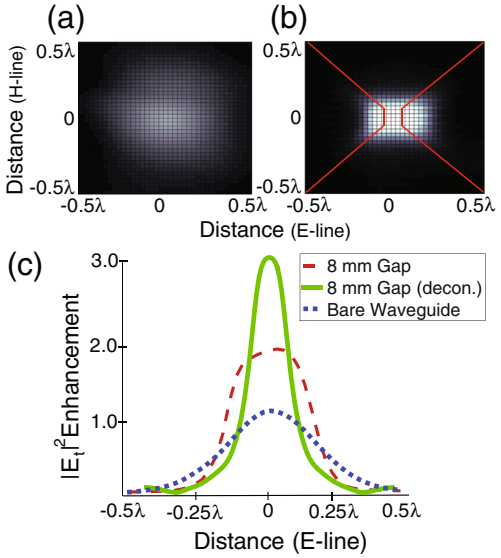

Fig. 4 Measured S_{21} **a** without and **b** with the bowtie. **c** $|E_t|^2$ enhancement pattern along X-axis

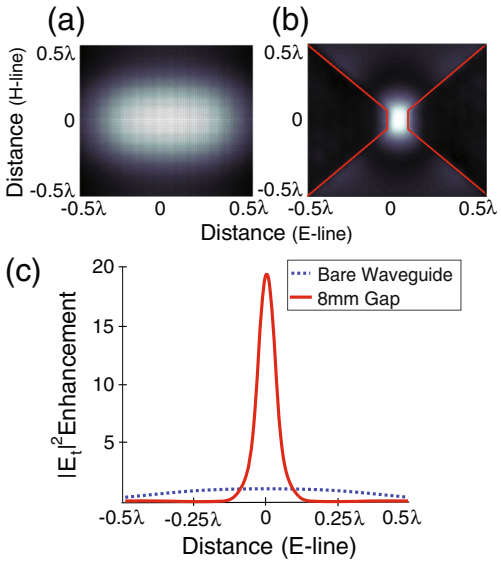

Fig. 5 Simulated electric field **a** without and **b** with the bowtie. **c** $|E_t|^2$ enhancement pattern along X-axis

is about 1.2 which is 40 % lower than this work. Figure 5 shows the NEC-2 simulation results, which support the experiment. NEC-2 results show an enhancement of 20 at the center of the bowtie in comparison with the simulation without bowtie (dotted line).

The receive antenna has a large effective length compared to the gap size. To compensate for this effect, the measured data has been de-convolved by the length of the antenna. In Fig. 4c, the solid line, which is the deconvolution of dashed line, shows three times $|E_t|^2$ enhancement.

Figure 6 shows the normalized transmitted electric field for the 45°, 90°, 135°, and 180° bowtie angle. Normalization has been done by comparing the measurement with the bowtie gap to the measured value at the center of the area of interest without the bowtie. As shown in Figs. 6 and 7, at 90°, the bowtie structure has the largest enhancement between all cases because it is the optimal tradeoff between the effective area and charge accumulation at the tips. A smaller angle ($< 90°$) would focus the charges at the tips more but the area receiving field energy would decrease. Moreover, at 90°, the bowtie antenna becomes self-complementary and has a stable impedance of 188 Ω [34]. With 90° plates, the transmitted electric field is a maximum for 0.08 λ gap size of the bowtie. For 45°, $|E_t|^2$ enhancement is a maximum at 0.06 λ, and for the rest (135° and 180°) there is no specific gap size where the enhancement is a maximum.

The other important parameter of the geometry of the gap is plate thickness. We investigate three different thicknesses (1/8", 1/4", and 3/8") to determine the effect of the plate thickness on the field enhancement. As long as the thickness of the gap plate is much bigger than the skin depth, we find that there is no significant difference between plate thicknesses. Skin depth of aluminum at 2.45 GHz is 1.65 μm, which is much thinner than the investigated plate thicknesses.

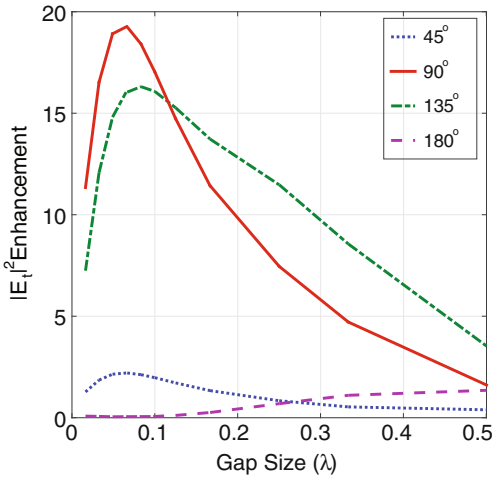

Fig. 7 Simulated $|E_t|^2$ enhancement over gap size

Discussion

As shown in the results, the $|E_t|^2$ increases by a factor of three from the experiment and by 20 from the NEC-2 simulation. According to [28], the amount of enhancement is affected by mode volume, coupling efficiency, and Joule losses. In our study, the mode volume is defined by the region where electric field is greater than $1/e$ (36 %) of its maximum. Stronger enhancement in simulation could be due to higher coupling efficiency and lower Joule losses compared to the experiment. The loss model in NEC-2 uses the concept of surface impedance. The model does not account for behaviors associated with fields within a good conductor. This simplified algorithm can result in discrepancy between measurement and simulation. In addition, the difference in the results at 45° between measurement and simulation needs further investigation. However, the behavior of the enhancement factor in both measurement and simulation agree with each other.

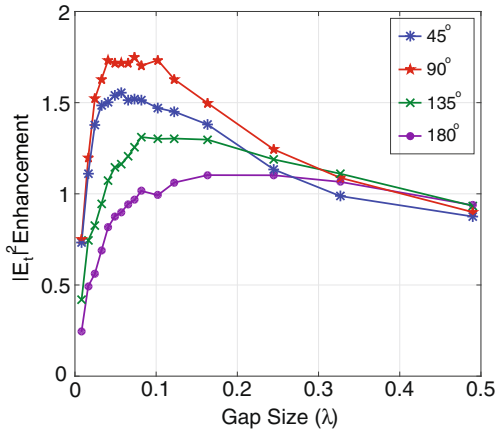

Fig. 6 Measured $|E_t|^2$ enhancement over gap size

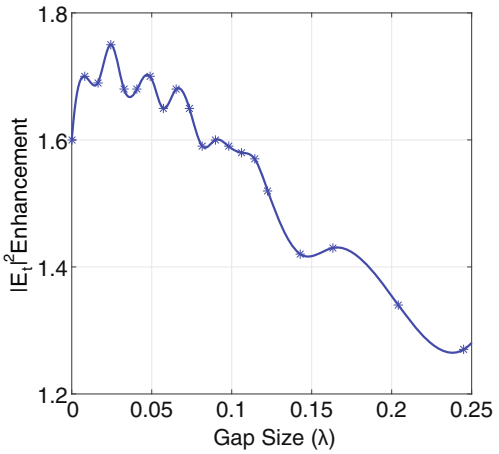

Fig. 8 Measured $|E_t|^2$ enhancement over gap size for graphite bowtie

We justify that our result from the macro experimental setup can be applied to design a nanoscale plasmonic device because aluminum is still highly reflective at optical frequencies. Also, a dielectric bowtie made of graphite is investigated at 2.45 GHz. Figure 8 shows similar results to the results of metallic gap. In this case, the maximum enhancement occurs at 0.02 λ gap size.

As [28] suggests, there is an inversely proportional relationship between enhancement and mode volume of the region. Therefore, enhancement can be significantly higher in nanoscale than seen in macroscale. Figure 9 shows the cross sectional views of the mode volume across the center of the bowtie gap. To acquire the mode volume precisely, electric field inside a $2 \times 3 \times 3$ cm^3 region around the $1 \times 1 \times 1$ cm^3 gap has been simulated on NEC-2. The mode volume is 8.43 cm^3 in this case. Therefore, the mode volume is 4.6×10^{-3} λ^3 and the product of the mode volume and enhancement factor is 7.4×10^{-2} λ^3. This result is in the same order as the results of [28] in nanoscale.

To study the effect of the tip width (denoted as l in Fig. 2), bowtie structure with sharp tips ($l \approx 0$) are used for the experiment and simulation. Figure 10 shows that the maximum enhancement occurs at the smallest gap size for bowtie structures with sharp tips. However, the sharper tips produce no additional enhancement in comparison with the flat tips. Thus, the curvature of the tip only affects the optimum gap size.

In nanoscale applications, plasmonic is used to detect a single molecule across the nanogap. We imitate the molecule detection by placing a semi-insulating material across the gap and measuring the field intensity change. Since different molecules and materials have different conductivity and permittivity, the charge accumulation on the tips of the bowtie structure is further studied by placing higher dielectric materials in the gap to change the capacitance. The enhancement increases by 10 % with acrylic ($\varepsilon_r = 1.9$), as shown in Fig. 11a. The measurement was performed with different resistors across the gap to change the conductance of the bowtie. As shown in Fig. 11b, the amount of enhancement decreases in the presence of the resistor. The impedance of the 90° bowtie is 188 Ω. Therefore, when the resistance across the gap is 200 Ω, most of the energy flows through the resistor and the enhancement factor is a minimum [Fig. 11b] [34]. A lower enhancement may indicate a conductive molecule at nanoscale.

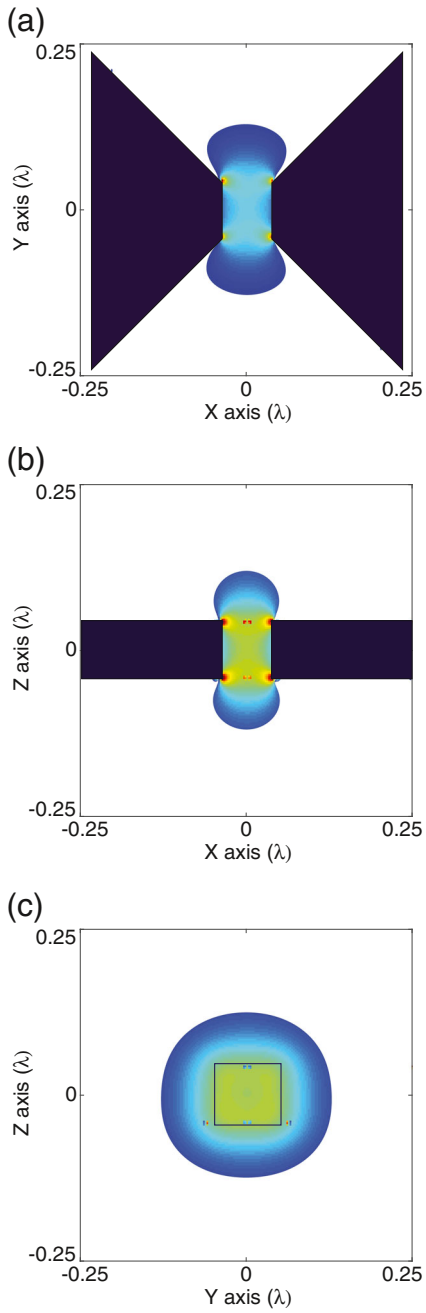

Fig. 9 Simulated electric field pattern for three cross-sections around the gap to estimate the mode volume

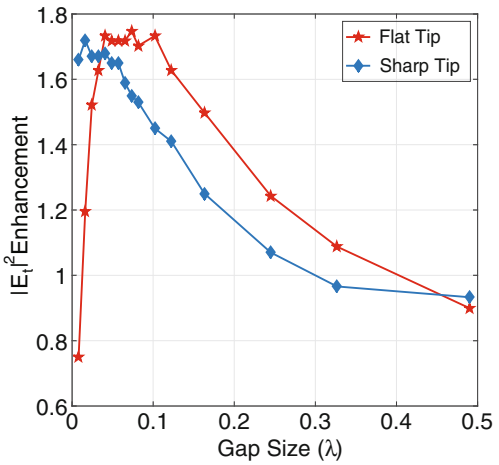

Fig. 10 Comparison of $|E_t|^2$ enhancement over gap size for flat and sharp bowtie tip

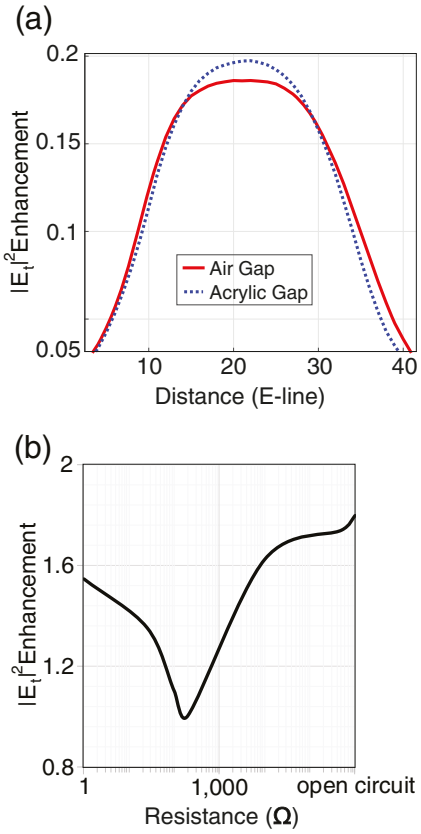

Fig. 11 Loaded gap results. **a** Effect of acrylic across the gap. **b** Enhancement factor for different resistors across the gap

Conclusion

In this work, we have measured the electric field enhancement across a bowtie gap at microwave frequency. Because the design and fabrication of the bowtie at nanoscale is challenging, we performed the experiment at macroscale to find the optimal geometry of the bowtie. The measurement results demonstrate the electric field enhancement is a maximum at a 90° bowtie angle and an 8 mm gap size in our study. Simulations were performed to confirm the results. The setup was further studied by placing a material with higher permittivity in the gap, which resulted in higher enhancement. We also showed conductivity of the material across the gap affects the enhancement. When the tip of the bowtie is sharper, the same magnitude of enhancement factor occurred at smaller gap size. Finally, we expect that our approach will be helpful for designing an ideal nanogap for a variety of plasmonic applications.

References

1. de Lange F, Cambi A, Huijbens R, de Bakker B, Rensen W, Garcia-Parajo M, van Hulst N, Figdor CG (2001) J Cell Sci 114:4153
2. Gramotnev DK, Bozhevolnyi SI (2010) Nature Photonics 4(2): 83
3. Betzig E, Lewis A, Harootunian A, Isaacson M, Kratschmer E (1986) Biophys J 49(1):269
4. Pohl DW, Denk W, Lanz M (1984) Appl Phys Lett 44:651
5. Betzig E, Harootunian A, Lewis A, Isaacson M (1986) Appl Opt 25(12):1890
6. Bouillard JS, Vilain S, Dickson W, Zayats AV (2010) Opt Express 18(16):16513
7. Berweger S, Weber JC, John J, Velazquez JM, Pieterick A, Sanford NA, Davydov AV, Brunschwig B, Lewis NS, Wallis TM, Kabos P (2015) Nano Lett 15(2):1122
8. Cricenti A, Generosi R, Luce M, Perfetti P, Margaritondo G, Talley D, Sanghera JS, Aggarwal ID, Tolk NH, Congiu-Castellano A, Rizzo MA, Piston DW (2003) Biophys J 4: 2705
9. Hinterdorfer P, Garcia-Parajo MF, Dufrne YF (2012) Acc Chem Res 45(3):327
10. Fang Y. (2015) Biosensors 5(2):223
11. Bohn BJ, Schnell M, Kats MA, Aieta F, Hillenbrand R, Capasso F (2015) Nano Lett 15(6):3851
12. Johnson JC, Yan H, Schaller RD, Petersen PB, Yang P, Saykally RJ (2002) Nano Lett 2(4):279
13. Khatib O, Wood JD, McLeod AS, Goldflam MD, Wagner M, Damhorst GL, Koepke JC, Doidge GP, Rangarajan A, Bashir R, Pop E, Lyding JW, Thiemens MH, Keilmann F, Basov DN (2015) ACS Nano 9(8):7968
14. Gan Q, Bartoli FJ, Kafafi ZH (2013) Adv Mater 25(17):2377
15. Moerner WE (2007) Physical principles and methods of single-molecule spectroscopy in solids:1–30
16. Xia T, Li N, Fang X (2013) Annu Rev Phys Chem 64(1):459
17. Walt DR (2013) Anal Chem 85(3):1258
18. Yeh HC, Chao SY, Ho YP, Wang TH (2005) Curr Pharm Biotechnol 6(6):453
19. Li J, Chen S, Yu P, Cheng H, Duan X, Tian J (2013) Opt Express 21(8):10342
20. Li J, Chen S, Yu P, Cheng H, Chen L (2012) J Tian, Plasmonics 8(2):495
21. Li J, Chen S, Yu P, Cheng H, Zhou W, Tian J (2011) Opt Lett 36(20):4014
22. Butet J, Brevet PF, Martin OJF (2015) ACS Nano 9(11):10545
23. Stewart ME, Anderton CR, Thompson LB, Maria J., Gray SK, Rogers JA, Nuzzo RG (2008) Chem Rev 108(2):494
24. Im H, Bantz KC, Lindquist NC, Haynes CL, Oh SH (2010) Nano Lett 10(6):2231
25. Kang M, Park SG, Jeong KH (2015) Sci Rep 5:14790
26. Liu Z, Boltasseva A, Pedersen RH, Bakker R, Kildishev AV, Drachev VP, Shalaev VM (2008) Metamaterials 2(1): 45
27. Giannini V, Fernñdez-Domnguez AI, Heck SC, Maier SA (2011) Chem Rev 111(6):3888
28. Kim MK, Sim H, Yoon SJ, Gong SH, Ahn CW, Cho YH, Lee YH (2015) Nano Lett 15(6):4102
29. Maier SA (2007) Plasmonics: fundamentals and applications. Springer, New York
30. Li EP, Chu HS (2014) Plasmonic nanoelectronics and sensing. Cambridge University Press, New York
31. Balanis CA (2012) Advanced engineering electromagnetics, 2nd edn. Wiley, New York
32. Grober RD, Schoelkopf RJ, Prober DE (1997) Appl Phys Lett 70:1354
33. Burke J, Poggio AJ (1980) Numerical electromagentics code (nec)-method of moments part 1, 2, and 3 in Report NOSC TD, vol 116. Naval Ocean Systems Center, San Diego
34. Stutzman WL (2012) Antenna theory and design, 3rd edn. Wiley, New York